Title: Spatial arrangement of the whiskers of harbor seals (*Phoca vitulina*) compared to whisker arrangements of mice (*Mus musculus*) and rats (*Rattus norvegicus*)

Running Title: Whisker array morphology of harbor seals, rats, and mice

Authors: Matthew M. Graff[1]
Hayley M. Belli[2†]
Sven Wieskotten[3††]
Chris S. Bresee[4†††]
Yvonne Krüger[3]
Thomas L. Janssen[1]
Guido Dehnhardt[3]
Mitra J.Z. Hartmann[1, 2]

Affiliations: [1] Department of Mechanical Engineering, Northwestern University, Evanston, Illinois, 60208, USA

[2] Department of Biomedical Engineering, Northwestern University, Evanston, Illinois, 60208, USA

[3] Institute for Biosciences, University of Rostock, Rostock, Germany

[4] Northwestern University Institute for Neuroscience, Northwestern University, Evanston, Illinois, 60208, USA

[†] Present address:
Department of Population Health, Biostatistics Division
Grossman School of Medicine New York University
New York, NY, 10016

[††] Present address:
Animal and Training
Postcode 30 10 43
18111 Rostock

[†††] Present address:
Center for Neuroscience
University of California, Davis
Davis, CA, 95616

Corresponding Author:
Mitra J.Z. Hartmann
Northwestern University
2145 Sheridan Rd
Evanston, IL 60208
hartmann@northwestern.edu
Tel: 847-467-4633

KEYWORDS: comparative anatomy, multimodal, flow sensing, trigeminal, whisker, somatosensory, touch

SUMMARY STATEMENT: We quantify the three-dimensional positions and orientations of the whiskers across the face of the harbor seal, and compare this geometry with the whisker arrays of rats and mice.

Abstract

Most mammals have specialized facial hairs known as vibrissae (whiskers), sensitive tactile structures that subserve both touch and flow sensing. Different animals have different numbers and geometric arrangements of whiskers, and it seems nearly self-evident that these differences would correlate with functional and behavioral use. To date, however, cross-species comparisons of three-dimensional (3D) whisker array geometry have been limited because standard morphometric techniques cannot be applied. Our laboratory recently developed a novel approach to enable quantitative, cross-species vibrissal array comparisons. Here we quantify the 3D morphology of the vibrissal array of the harbor seal (*Phoca vitulina*), construct a CAD model of the array, and compare array morphologies of harbor seals, mice (*Mus musculus*) and rats (*Rattus norvegicus*). In all three species whisker arclength decreases from caudal to rostral, whisker curvature increases from caudal to rostral, and whiskers emerge from the face in smooth orientation gradients. Two aspects of whisker orientation are strikingly consistent across species: the elevation angle is constant within a row, and the twist of the whisker about its own axis varies smoothly in a diagonal gradient across the array. We suggest that invariant whisker elevation within a row may aid localization behaviors, while variable twist-orientation may help the animal sense stimulus direction. We anticipate this work will serve as a starting point for quantitative comparisons of vibrissal arrays across species, help clarify the mechanical basis by which seal vibrissae enable efficient wake detection and following, and enable the creation of whole-body biomechanical models for neuroscience and robotics.

1. Introduction

Nearly all mammals have specialized hairs known as vibrissae (whiskers) that protrude from the mystacial pad in a regular grid-like pattern (Ahl, 1986; Muchlinski, 2010a; Muchlinski et al., 2020). Along with olfactory specialization, whiskers were likely one of the earliest sensory adaptations particular to stem mammals (Rowe et al., 2011). The vibrissal arrays of different species have evolved to have different numbers of whiskers as well as distinct shapes, sizes, and arrangements (Burns, 2009; Danforth, 1925; Grant et al., 2013b; Muchlinski, 2010a). The morphology of individual whiskers differs between species as well. For example, house mice (*Mus musculus,* "mouse") and Norway rats (*Rattus norvegicus,* "rats") have nearly-conical, tapered whiskers (Belli et al., 2018; Hires et al., 2016; Williams and Kramer, 2010), while harbor seals (*Phoca vitulina*, "seals") have whiskers with elliptical cross-sections, undulated in a manner that helps minimize vortex shedding while swimming (Ginter et al., 2012; Ginter et al., 2010; Hanke et al., 2010; Hans et al., 2013).

Whiskers are classically studied as active sensors, with different species varying in their ability to "whisk," a behavior in which the animal rhythmically protracts and retracts its whiskers to acquire tactile information (Welker, 1964). Mice and rats can generate exceptionally strong whisking behaviors, with specialized intrinsic muscles allowing large (30 – 40 deg) amplitude whisker rotations (Carvell et al., 1991; Dörfl, 1982; Haidarliu et al., 2015; Haidarliu et al., 2010; Muchlinski et al., 2013). In contrast, many carnivores, such as harbor seals and cats (*Felis catus*), have "mobile" whiskers that allow bilateral adjustment of overall position, but do not exhibit rhythmic whisking behavior (Dehnhardt and Kaminski, 1995; Grant et al., 2013a; Woolsey et al., 1975).

These species-related differences in whisker number and geometry, array morphology, and whisking ability seem likely to be associated with differential functional use of the whiskers. For example, terrestrial rodents use their whiskers primarily for direct touch (Brecht et al., 1997; Carvell and Simons, 1990; Welker, 1964), though they can also use them for indirect touch to sense the direction of airflow (Mugnaini et al., 2023; Yu et al., 2016). In contrast, seals primarily use their whiskers for indirect touch, sensing vibrations to track wakes while hunting fish (Dehnhardt et al., 1998; Dehnhardt et al., 2001; Hyvarinen, 1989; Kruger et al., 2018; Miersch et al., 2011; Schulte-Pelkum et al., 2007; Wieskotten et al., 2010; Wieskotten et al., 2011), though they can also use them in tactile discrimination tasks (Dehnhardt and Kaminski, 1995; Grant et al., 2013a).

To date, however, many relationships between vibrissal array morphology and functional use remain unexplored, largely because landmark or semi-landmark based morphometric approaches (Bookstein, 2018; Shui et al., 2023) cannot be used to compare geometries across species with very different numbers and arrangements of whiskers. New quantitative methods are required.

Our laboratory recently developed a head-centered approach to quantitatively compare 3D facial and whisker array morphology across species (Belli et al., 2018). In this approach the coordinates of each facial feature, including the whisker basepoints, are identified within a head-centered coordinate system. The whisker basepoints are then used as independent variables to generate equations that quantify the geometry of individual whiskers and of the whisker array. The present work uses this approach to quantify the morphology of the whisker

array of the harbor seal and compare it with the morphologies of mice and rats. A 3D scan of a seal's face is then used to place the whisker array in the context of other facial features, including the eyes and snout, to generate a CAD model for use in robotics and fluid mechanics experiments.

The contributions of this work are threefold: first, we anticipate that it will serve as a starting point for quantitative comparisons of vibrissal array geometry across species; second, that it will help clarify the mechanical basis by which seal vibrissae enable efficient wake detection and following; and, finally, that it will aid in the creation of whole-body biomechanical models for use in neuroscience and robotics.

2. Methods

2.1 Animals, housing, and training

Three awake, behaving, adult, male harbor seals were used to quantify whisker and whisker array morphology. At the time of data collection Seal 1 (Filou, born 2006) was 5 years old, Seal 2 (Sam, born 1994) was 14 years old, and Seal 3 (Henry, born 1997) was 17 years old.

All seals resided at the Marine Science Center of Rostock University in Hohe Düne, Germany. The center is located within a marina, and consists of a moored ship (length 40 m) that serves also as an office building. The animals were kept in a mesh-surrounded 1,800 m^2 main enclosure around the ship with a maximum depth of 6 m, constantly provided with fresh seawater. Floating pontoons within the animal enclosure offer space for the animals to haul out of the water. The animals were fed approximately 80% of their daily diet (about 2 kg of freshly thawed fish cut herring or sprats per day, supplemented with vitamins) during experimental sessions as primary reinforcement.

Experiments were conducted once per day, five days per week. At the time of the experiment all animals had previously been trained to "station" from an early age, to keep their head motionless at a cued point in space for an extended duration. This established behavioral training was the only technique used to facilitate immobility during whisker measurements, therefore the tone of the facial muscles likely varied somewhat between individuals and between scans. Although we have no measurement of degree of activation of vibrissal-related facial muscles, we qualitatively judged that vibrissae were in a neutrally relaxed position (neither retracted nor protracted) and generally in equivalent positions across scans and across animals, based on visual assessment of the data. Quantification of whisker emergence angles (*Results*) later confirmed the similarity across individuals. The reproducibility in emergence angles is unsurprising due to the highly stereotyped nature of the well-trained and frequently repeated stationing behavior.

All experiments performed at the Marine Science Center of Rostock University were conducted in accordance with the European Communities Council Directive of 24 November 1986 (86/609/EEC), the directive 2010/63/EU and the Directive of the §7 and §11 TierSchG of the German Protection of Animals Act (Tierschutzgesetz).

2.2 Data acquisition

The head and vibrissal array of each seal were scanned using a (3D) volumetric scanner. A total of 361 3D whisker images were taken of 171 unique whiskers. Additionally, 127 two dimensional (2D) images were taken of 52 unique whiskers.

2.2.1. Three-dimensional volumetric scanning and data extraction: A Konica Minolta Vivid 900 non-contact, 3D laser scanner was used to acquire 3D scans. The resolution of the scan depends on distance to the subject and the time of the scan, which necessarily varied slightly due to the exigencies of work with awake behaving animals. The scanner can acquire up to ~300,000 points in 2.5 seconds, and this can be done in a ~10x10 cm box at a range of ~5 cm, and up to a ~100x100 cm box at a range of ~75 cm. Each seal was trained to pose its head on a semicircular stand (a chinrest) for a duration of less than one minute (one to two scans). The seal's eyes were covered with a thick, opaque rubber mask during laser scanning. An example of a blindfolded seal resting its head on the chinrest is shown in Fig. 1A. The scanner output was a digitized point cloud. The software package Rapidform™ XOR2 was used to control the scanner from a laptop computer. The point clouds included portions of the seal's head, neck, and whiskers. The seal's head and whisker arrays were larger than the field of view of the scanner, so multiple scans in several orientations were taken and then combined in post processing.

2.2.2. Two-dimensional photographs: All photographs of whiskers were taken when animals voluntarily and transiently chose to emerge from the sea enclosure around the ship, so the whiskers were in a hydrated state. Hydration state is important when estimating intrinsic whisker curvature because informal observation indicates that a whisker's shape changes rapidly and substantially as it dehydrates, on the time scale of ~20 minutes.

Because whiskers could not be plucked from the animal, photographs of the whiskers were taken against a black, hard-plastic background. A camera-frame system (Fig. 1B) was constructed to ensure that the whiskers lay flat on the background with no distortion of their natural shape. The frame system, constructed of 80/20®, also ensured a fixed distance between the camera (Panasonic, Lumix DMC-FZ20) and the background, and resulting photographs had a resolution of ~200 microns/pixel. Length scales (thin plastic rulers) were affixed rigidly to the background.

The 2D photographic procedure was as follows: A select number of whiskers were marked using non-toxic watercolor paint. The background was then manually held against the face of the seal in an orientation such that one selected whisker lay flat against the background without any shape distortion. Although several whiskers (painted different colors) were often visible in each photo, the frame was oriented so that one specific whisker lay completely flat. During analysis, we could be confident that we captured the entire arclength of the whisker because the tip of each whisker was clearly visible with the naked eye against the dark black background in the digital photograph. An example of a typical 2D photo of a whisker with a blue stripe is shown in Fig. 1C. The photo in Fig. 1D shows how the frame was oriented by hand to position the whisker onto the background.

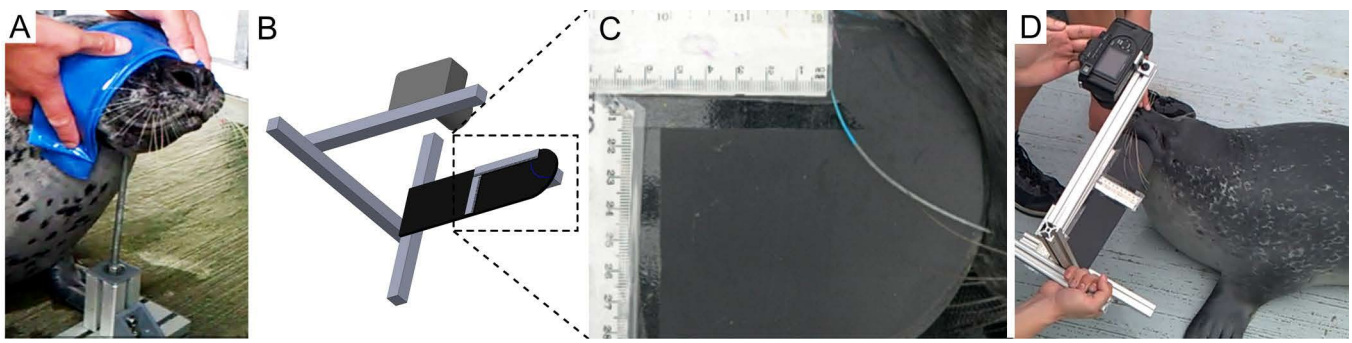

Fig. 1: The head and vibrissal array of a harbor seal were scanned in 3D and 2D. Photos have been brightened and contrast enhanced to improve clarity. **(A)** A blindfolded seal is shown perching its head on a chinrest to permit 3D laser scanning. **(B)** A schematic of the custom-built camera frame system, which allowed the whisker to be photographed in 2D. The orientation of the background was manually adjusted so that the whisker of interest lay flat on the background. **(C)** An expanded view of the camera frame system shows an exemplary 2D photograph of a whisker identified with non-toxic watercolor paint. **(D)** A photo shows how the custom-built camera frame system was used in practice.

A log of the correspondence between painted color and whisker identity was recorded as the photographs were taken, and the images of the seal whiskers were then imported into Matlab™ (The Mathworks, Natick, MA) for measurement. The shapes of the whiskers were manually extracted by clicking on the center of the whisker along its length, from base to tip. After clicking along the entire whisker, the traces were up-sampled (linear interpolation) to contain 100 points and smoothed using a moving average filter with a window size of 15 samples. All whisker traces were overlaid onto the original photographs and manually inspected for accuracy. All traces were converted to real-world length units using the scale bars attached to the background (Fig. 1C). Note that the present manuscript quantifies the "arclength" (S) of the whisker, which is the length of the whisker along the curve of the whisker. The "arclength" is different from the chord length that describes the straight line between the whisker's base and its tip.

2.3 Alignment of three-dimensional data

Alignment of the 3D data required three basic steps.

First, in order to assign identities to each of the whiskers, we performed a coarse alignment of the point clouds within Rapidform™. Data points associated with the head or neck or with scanner noise were manually removed. The most complete point cloud for each seal was chosen as the reference scan. All other scans were rotated and translated to align to the reference scan using facial landmarks. Landmarks included whisker basepoints, the nostrils, and creases in the face and mouth. Whiskers were identified by their location within the array (Dehnhardt and Kaminski, 1995) as well as by comparing the point clouds to photographs of the full mystacial pad of the seal. All data points corresponding to each individual whisker were saved into their own point clouds.

Second, we localized the basepoints of all identified whiskers. For each whisker point cloud, the basepoint was identified by finding the intersection between the whisker and the skin in Rapidform™. In nearly all cases the proximal portion of the whisker and the skin were both clearly visible. If the basepoint was not identifiable in a particular whisker scan, that scan was removed from the dataset and not used for further analysis. The whisker-skin intersection of the point cloud was typically composed of 5 to 15 points. The centroid of these points was used as the basepoint location.

At this point in the alignment process, each 3D scan of a particular seal now consists only of point clouds of identified whiskers, and each whisker point cloud has an average basepoint. All non-whisker related points have been removed, ensuring that the automated alignment described in the next step included only the appropriate whisker-related points.

The third step was to perform fine alignment of these “whisker-and-basepoint-only” scans. As before, the scan with the largest number of basepoints was used as the reference scan. An optimization was performed using the “fminsearch” function in Matlab™ in which each of the “whisker-only” scans was rotated and translated into alignment with the reference scan. The objective function for the minimization consisted of the summed distances of all matching basepoints between the reference scan and each individual scan. The goal of this step was to align all scans from a single seal. This step was necessary because we could only scan from one perspective at a time; multiple scans of the same animal were required to form a full 3D representation of an individual array. Note that we never aligned scans from multiple individuals.

2.4. Overview of the head-centered morphology approach and description of variables

The head-centered approach to quantify 3D facial and whisker array morphology has been described previously (Belli et al., 2018; Bresee et al., 2023), and involves three basic steps. First, an origin and horizontal plane are chosen based on selected features of the animal’s face and/or skull. Because the present work focused on the vibrissae, we chose the mean of all whisker basepoints as the origin, and the “average row plane” of the whiskers to define horizontal. Second, the positions of all facial features of interest – in this case the whisker basepoints (r_{bp}, θ_{bp}, ϕ_{bp}) – are identified within this head-centered coordinate system. Modified spherical coordinates are used because they adapt most naturally to the (roughly spherical) geometry of an animal’s head. The variable θ_{bp} describes the horizontal basepoint location, ϕ_{bp} describes the elevation basepoint location, and r_{bp} is the straight-line distance between the origin and the basepoint. Writing an equation for r_{bp} in terms of θ_{bp}, ϕ_{bp} quantifies the overall 3D shape and size of the whisker array.
.
In the third step, the two angular basepoint coordinates are used as independent variables to generate equations for the parameters of individual whiskers and their arrangement on the face. Individual whisker parameters include arclength (S) and intrinsic curvature (A), as well as diameter (D) and diameter as a function of arclength (taper). In the case of the harbor seal, whiskers have non-circular cross-sections and undulations, so additional parameters include major and minor diameter axes and the 3D angles that quantify undulations along the whisker length. Because the present study was performed in awake behaving animals, estimates of diameters and undulations were not obtained; only arclength and intrinsic curvature were quantified. The arrangement of each whisker on the face is defined by its position (given by its basepoint coordinate), and the 3D orientation at which it emerges from the mystacial pad (“emergence angles”). Here, the emergence angles are defined by three Euler angles (θ_w, ϕ_w, ζ_w) and a convention for the order of rotation.

These three steps allow us to write equations for r_{bp}, S, A, θ_w, ϕ_w, ζ_w in terms of θ_{bp} and ϕ_{bp}, so that the equations describing the whiskers and whisker array geometry can be compared across different species. We note that the approach can also be used to parameterize the locations of facial and skull features.

2.5 Choice of origin and horizontal plane: standard position and orientation of the head

To place the head into a standard position, we chose the mean of all whisker basepoints as the origin. To do this, we translated the aligned point clouds so that the origin was located at the mean position of all right and left whisker basepoints. This puts the origin inside the animal's head, near the center of the muzzle (Fig. 2A). This procedure was implemented using "matched" basepoints between right and left sides; in the case that a basepoint was missing on one side, its non-missing complement was omitted from the calculation of the origin. For seals with multiple measurements of the same basepoint, the mean of the points was used for the alignment procedures.

To put the head into a standard orientation, we used the "average row plane" of the whiskers to define horizontal. We performed a roll-yaw-pitch (y-z-x-axis) rotation sequence. The roll rotation (about the y-axis) and the yaw rotation (about the z-axis) placed the center of the right array on the positive x-axis and the center of the left array on the negative x-axis (Fig. 2A). The "center" of the right (left) array is defined as the mean of all basepoint positions on the right (left) side of the animal.

The pitch rotation (about the x-axis) aligned the average whisker row plane with the x-y (horizontal) plane. To find the average whisker row plane, individual planes were fitted to the basepoints of the combined left and right whisker rows using least squares and producing six normal vectors – one for each of the six whisker rows B - G. The A row of whiskers was excluded because it contained an insufficient number of points to define a plane. The maximum sum-squared-error between the basepoints and its fitted plane was 90.2 mm^2 (maximum residual was 5.5 mm). The mean of the unit normal vectors describes the average row plane (Fig. 2B). The animal's head was then pitched about the x-axis so that the average row plane was parallel with the x-y plane. The final position of the seal point cloud is shown in Fig. 2C.

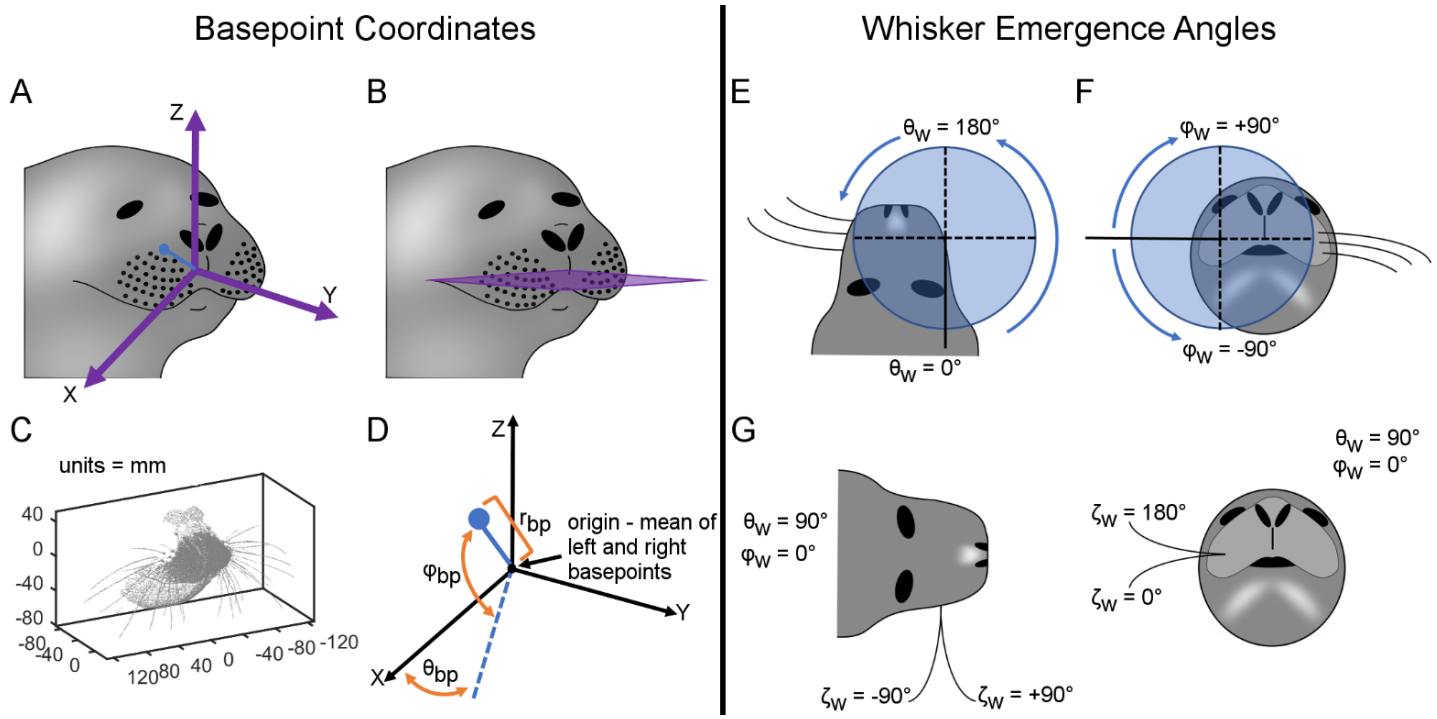

Fig. 2: Coordinate systems for whisker basepoints and emergence angles are defined in schematics. (A) Schematic of the standard position and orientation of the vibrissal array. The origin (0,0,0) is placed at the mean position of the basepoints of the left and right array. The right basepoints surround the positive x-axis. The blue line and dot indicate a single example of a basepoint location, for comparison with panel (D). **(B)** The horizontal (x-y) plane is defined by the average row plane of the basepoints. **(C)** An example point cloud of a seal's face in the standard position and orientation. **(D)** Each basepoint location is described in spherical coordinates (θ_{bp}, ϕ_{bp}, r_{bp}). The angle θ_{bp} ranges from -90° (caudal) to +90° (rostral), where θ_{bp} = 0° lies in the x-z plane. The angle ϕ_{bp}

ranges from -90° (ventral) to +90° (dorsal), where ϕ_{bp} = 0° lies in the x-y plane. The basepoint coordinates of one example whisker (blue dot) are shown. **(E)** The variable θ_w describes the rostrocaudal angle at which the proximal, approximately-linear portion of the whisker emerges from the mystacial pad. Values range from 0° to 360°. **(F)** The variable ϕ_w describes the dorsoventral angle at which the proximal, approximately-linear portion of the whisker emerges from the mystacial pad. Values range from -90° to 90°. **(G)** The variable ζ_w describes the twist of the whisker about its own axis. Values range between ±180°.

2.6 Coordinates of the whisker basepoints and area of the pad

The seal whisker array is organized in a grid-like pattern that includes 7 rows and 9 columns (Dehnhardt and Kaminski, 1995). In contrast, the rat's whisker array is organized in a grid-like pattern that includes 5 rows and 7 columns (Belli et al., 2018; Brecht et al., 1997; Knutsen et al., 2008; Towal et al., 2011). For both the seal and the rat, a whisker is identified with a letter indicating its row and a number indicating its column. In the present study, however, we chose to quantify the morphology of the seal whisker array in terms of the coordinates of the whisker basepoints, rather than row and column identity.

Basepoint coordinates were determined within a spherical coordinate system (Fig. 2D) with the origin located at the mean position of all the basepoint locations (Fig. 2B). For each whisker, the variable θ_{bp} describes the rostro-caudal location of the basepoint with respect to the positive x-axis. A positive value of θ_{bp} indicates that the whisker is more rostral, while a negative angle indicates that the whisker is more caudal. The variable ϕ_{bp} describes the dorsoventral location of the basepoints with respect to the x-y plane. A positive value of ϕ_{bp} indicates a more dorsal basepoint location, while a negative coordinate indicates a more ventral basepoint location. The third basepoint coordinate is the radius (r_{bp}), i.e., the straight-line distance between the origin and the basepoint. Scaling the basepoint radii scales the size of the seal's face.

For mathematical simplicity, whisker arrays on the left side were converted to right side arrays by mirroring them across the y-z plane. All equations and figures are presented in terms of whisker arrays on the right side. The advantage of this choice of coordinate systems is that it intuitively exploits the bilateral symmetry of the array.

To generate an estimate of surface area of the whisker array we first found the mean position of each whisker basepoint across all seals. We then found the residuals of each basepoint (from individual seals) from its corresponding mean. Next, we manually connected three adjacent basepoint identities to form a trimesh of non-overlapping triangles that covered the entire whisker pad surface. The whisker array area was computed as the sum of the areas of these triangles. The range for the area was computed by computing the surface area using the mean plus and minus the extreme values of the residuals in all directions.

2.7 Measurements of whisker arclength and intrinsic curvature using two-dimensional data

The arclength (S) of each whisker was calculated by summing the lengths of the segments that composed the traced image in each 2D photograph.

The intrinsic curvature of the whiskers of ten different animal species, including the harbor seal, has been quantified in detail in Luo and Hartmann, 2023. This previous study found that a fractional exponent model may be best suited for describing whisker shape. In the present work, however, we aimed to describe intrinsic curvature in the simplest and most intuitive way possible.. Therefore, following established methods (Belli et al., 2018; Bresee et al., 2023; Knutsen et al., 2008; Towal et al., 2011), each whisker was fit using a single "curvature coefficient," based on a polynomial fit.

Each seal whisker was fit with both quadratic and cubic curves, and then visually assessed for goodness of fit. Cubic fits were found to be a far better match, as they accommodated the linear proximal portion while also capturing most of the curvature in the distal portion. In its most general form, a cubic polynomial has four coefficients: $f(x) = Ax^3 + Bx^2 + Cx + D$. For simplicity, we forced the B, C, and D coefficients to exactly equal zero, and performed a least-squares regression to the curve $f(x) = Ax^3$. This alignment procedure requires the proximal portion of the whisker to be aligned with the x-axis. To achieve this alignment, the whisker was first divided into 100 nodes. The whisker basepoint was then placed at the origin (0,0) and the next proximal mode (~1% of the whisker arclength) was aligned with the x-axis. This procedure offers the advantage that only a single coefficient, with an intuitive meaning, is required to describe the intrinsic curvature of the whisker.

2.8 Angles of emergence

The orientations of the whiskers as they emerge from the mystacial pad are termed the emergence angles (Towal et al., 2011). In the present work, we describe these angles using Euler angles (specifically Tait-Bryan angles) applicable to the right array. The emergence angles were measured from 3D scans obtained with the whiskers in a neutrally relaxed position. Given that the seal whisker array is mobile, these angles reflect only one possible position for the whiskers. Future work could use the 3D model developed here to simulate and quantify the effects of whisker motion and angle changes on the mechanics of sensory acquisition behaviors and wake following.

The horizontal angle θ_w describes the rostrocaudal orientation of the proximal portion of the whisker. A θ_w angle of 180° is directed rostrally while an angle of 0° is directed caudally (Fig. 2E). The elevation angle ϕ_w describes the dorsoventral orientation of the proximal portion of the whisker. A ϕ_w angle of 90° points the whisker dorsally while an angle of -90° points it ventrally (Fig. 2F). Whiskers have an intrinsic curvature and therefore they require a third angle, ζ_w, to describe the roll about their own axis. For a whisker with $\theta_w = 90°$ and $\phi_w = 0°$, a ζ_w angle of 90° will curve concave forward and -90° concave backward (Fig. 2G). In contrast, a ζ_w angle of 180° will curve concave upward, and 0° concave downward (Fig. 2H). Note that the directionality of the whisker's concavity in the head-centered coordinate system is defined by all three orientation angles, not just ζ_w.

As was true for the basepoint coordinates, the emergence angles are defined only for whiskers of the right array. For simplicity, all left side whisker arrays were converted to right side arrays by reflecting them across the y-z plane.

An optimization was performed using the built-in Matlab™ function "fmincon" to calculate the angles of emergence. The parameters for the optimization were θ_w, ϕ_w, ζ_w, along with S and A. Constraints on the angles of emergence in the optimization were: θ_w = [0, 360], ϕ_w = [-90, 90], ζ_w = [-180, 180], S = [straight distance from base to tip, lower bound + 50mm], curvature coefficient A = [0 to 1]. The curvature coefficient A was constrained to lie between 0 and 1. The lower bound for S was chosen to be the linear distance between the base and tip (the smallest S could ever possibly be to connect those two points) and 50 mm longer than the lower bound. Beginning with the whisker point cloud in standard position and orientation (Figs. 2ABC), the individual points within the cloud were sorted by distance from the basepoint.

Their x, y, z coordinates were then smoothed with a moving average filter (window size of five samples). The whisker was resampled into 500 micron segments and translated to have the base at the origin. The routine subsequently varied five variables, θ_w, ϕ_w, ζ_w, S, and A to fit an idealized whisker model to the whisker point cloud. The idealized model started with the base at the origin ($\theta_{bp} = 0$, $\phi_{bp} = 0$, $r_{bp} = 0$), and the proximal section of the whisker was coaxial to the negative y-axis ($\theta_w = 0$, $\phi_w = 0$). The model's orientation was concave down ($\zeta_w = 0$). To align the idealized model with the whisker point cloud, an Euler rotation sequence was performed. The order of the rotations was y-axis (roll, ζ_w), x-axis (pitch, ϕ_w), z-axis (yaw, θ_w). All rotations were extrinsic around the global y-x-z axes. Additionally, the arc-length and curvature were optimized to best match the idealized model to the point cloud. The optimization's objective function minimized the mean sum squared distance between the whisker point cloud and the points in the idealized whisker model.

2.9 Developing equations for morphological parameters; statistical analysis

We aimed to develop equations that relate whisker arclength (S), intrinsic curvature (A), the angles of emergence (θ_w, ϕ_w, ζ_w) and the radial distance of each basepoint ($\mathbf{r_{bp}}$) to the locations of the whisker basepoints θ_{bp} and ϕ_{bp}. Model selection followed the procedures described in Bresee et al., 2023, and can be briefly summarized in four steps. First, we made individual models for each seal, so as to avoid overfitting by treating each whisker from an individual array as an independent measurement. Second, we used forward selection to increase the complexity of the model, adding predictor variables and higher order variables. Third, if the more complex model had a lower Akaike Information Criterion (AIC) by at least two points, it was accepted and the process of forward selection was repeated, otherwise the less complex model was accepted. Fourth, after finding the best fitting equations for each individual, we used the form of equation that best fit the most individuals, and applied that to the entire pooled dataset.

2.9.1. Arclength and intrinsic curvature as functions of θ_{bp} and ϕ_{bp}

The procedures described in sections 2.1 to 2.6 yielded a total of 171 unique 3D images of whiskers from three individual seals. However, when these 171 whiskers were compared across individuals, several whiskers were found to have unusually short arclengths given their identity. The short arclength was attributable to two causes. First, in some scans, the 3D scanner did not have sufficient spatial resolution to capture the full length of the whisker. Second, we performed the scans during the summer months, when two seals were undergoing vibrissal renewal and replacement (Hirons et al., 2001) and some of the whiskers had not fully regrown.

Rather than fit a model that under-predicts S and inaccurately predicts A, we excluded the data for S and A from the 3D scans, and instead constructed multivariate linear regressions models for S and A as functions of θ_{bp} and ϕ_{bp} using only the 2D dataset of 52 unique whiskers. For these 2D data, scan quality did not contribute significantly to measurement error in the arclength, as was the case for the 3D scans. The unusually short 2D measurements were attributable only to vibrissal renewal and replacement. To determine outliers due to vibrissal renewal and replacement, any whisker from the 2D data (from a particular seal) that was more than 30 mm shorter than the longest whisker (across all seals, for that whisker identity) was excluded. This threshold captures values greater than two standard deviations from the mean whisker length. Eight of the 52 2D traces were excluded based on this criterion, and the remaining 44 2D whiskers were then used to find relationships between S, A and θ_{bp} and ϕ_{bp}.

Among the 44 whiskers used in constructing the 2D model, 27 came from Seal 1, 13 from Seal 2, and four from Seal 3. Using the reduced set of 44 whiskers, first-order models for the log-transformed 2D arclength (S) and cubic coefficient (A) were fit as functions of θ_{bp} and ϕ_{bp}. Because 2D traces did not provide basepoint coordinate measurements, the average basepoint coordinates from the 3D scans were matched to the whisker identity of each 2D trace.

Even though there are fewer 2D measurements than 3D measurements for S and A, we can be confident that they capture the full length of the whisker and will therefore more accurately depict the cubic coefficient. Therefore, results for arclength and cubic coefficient (Fig. 5 and equations 2, 3, and 4) are based only on the 2D data.

2.9.2. Angles of emergence (θ_w, ϕ_w, and ζ_w) and r_{bp} as functions of θ_{bp} and ϕ_{bp}

As described above, some of the whiskers from the 3D images were found to have unusually short arclengths. However, we did not remove any whiskers when finding equations for θ_w, ϕ_w, ζ_w, and r_{bp} as functions of θ_{bp} and ϕ_{bp}, because we fully expect whiskers at various stages in the growth cycle (i.e., with various lengths) to retain the same emergence angles.

We aimed to construct multivariable linear regression models for r_{bp}, θ_w, ϕ_w, and ζ_w as functions of θ_{bp} and ϕ_{bp}. Rather than fit a model directly to the entire dataset of 171 whiskers and potentially overfit the data, we wanted to first find the lowest order model that could fit all three seals individually, and then apply a model of same order to the entire dataset of 171 whiskers.

We constructed models using the method of forward selection and evaluation based on AIC, first finding the best fit model for each individual and then applying the most common model form to all individuals together. We first divided the data from 171 whiskers for r_{bp}, θ_w, ϕ_w, and ζ_w into three subgroups by seal identity. For each of the three seals, we made histograms for r_{bp}, θ_w, ϕ_w, and ζ_w. All 12 histograms were found to be normally distributed. Linear regression models were constructed for each seal to test whether r_{bp}, θ_w, ϕ_w, and ζ_w were univariately associated with θ_{bp} and/or ϕ_{bp}. We tested the hypothesis that the θ_{bp} and/or ϕ_{bp} regression coefficients were equal to zero. If the p-value for each independent variable coefficient was less than 0.05 we tested a second order model (square of θ_{bp} and/or square of ϕ_{bp}), but only accepted the higher order model when it also had a p-value <0.05 and an AIC of at least 2 points lower than the lower order model. If the second order model was significant and supported by a lower AIC, a third order model (cube of θ_{bp} and/or cube of ϕ_{bp}) was tested, and accepted if it had a p value <0.05 and at least a 2-point lower AIC than the quadratic model. We did not find any models for whiskers from an individual seal to have independent variable predictors greater than third-order.

Using the procedure described above, the lowest order model among the three seals with significant regression coefficients was selected as the final model. As will be shown in the results, we found r_{bp}, θ_w, and ζ_w to be linear

in both θ_{bp} and ϕ_{bp}, and ϕ_w to be linear in ϕ_{bp} only. These final selected models were fitted to the entire combined dataset of 171 whiskers across all three seals.

2.10. A complete 3D scan of the seal head and facial features obtained from a fourth, deceased animal

The 3D laser scans of the live seals were focused closely on the whiskers, and the seals were blindfolded during the scanning. Therefore, the scans of the live animals contained limited information about the location of many facial features. We therefore performed a 3D laser scan of the head of a deceased adult, male harbor seal obtained from *Allied Whale* at the College of the Atlantic in Bar Harbor, Maine. A Keyence Romer arm 7525 S1 was used to take multiple scans of the head, which were then merged within the software Geomagic™. The head was scaled and aligned with a 3D scan obtained from one of the live seals to place the whisker array in the context of other facial features, including the eyes, nostrils, and mouth. Data were exported as a CAD file. The tissue transfer was approved in advance by the Institutional Animal Care and Use Committee of Northwestern University and the work was performed with authorization from the U.S. National Oceanic and Atmospheric Administration's (NOAA's) National Marine Fisheries Service (NMFS) in accordance with the U.S. Marine Mammal Protection Act regulations.

3. Results

3.1. The overall size and shape of the mystacial pad of the harbor seal

For the adult, male harbor seals considered here, the whisker basepoints of a single array encompass a surface area of ~15 ±2.8 cm^2 on the cheek (Figs. 3AB). To gain intuition for array size, it is helpful to compare the seal array to that of the rat (Fig. 3C). The seal array is approximately 10 times larger in surface area than the rat array, in which the basepoints occupy an area of ~1.4 ±0.35 cm^2 (data from Belli et al., 2018), and 30 times larger than the mouse array, with an area of just ~0.5 ±0.16 cm^2 (data from Bresee et al., 2023). The seal array also spans a greater medial-lateral extent on the muzzle, so that its most rostral whiskers have larger values of θ_w. The most rostral whiskers of the seal cross 180° (c.f., Fig. 2E) and point inward toward the midline of the head.

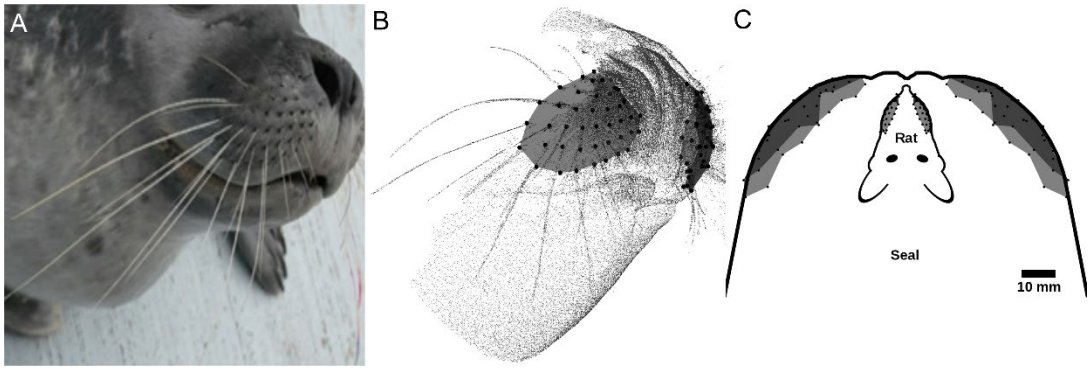

Fig. 3: Images of the harbor seal mystacial pad show the overall size and shape of the whisker array. A) A photograph of the seal mystacial pad and whiskers. **B)** The basepoint surface (a trimesh of whisker basepoints) is overlaid on the 3D scanned point cloud. **C)** Top-down views compare rat and seal arrays.

3.3 Basepoint coordinates

Previous studies have characterized the qualitative shape of the harbor seal whisker array, as well as whisker identities within the array (Dehnhardt and Kaminski, 1995), as shown in Fig. 4A. Plotting ϕ_{bp} vs. θ_{bp} yields a quantitative depiction of the array that closely resembles the qualitative description (Fig. 4B). In particular, the discontinuity in row direction between columns 4 and 5 is maintained in the quantitative description, although it is evidenced as a gradual bend in direction rather than a sudden break.

The basepoint coordinate θ_{bp} was used as an independent variable to quantify the radial coordinate of the basepoints (r_{bp}). Results are shown in the first line of Table 1 and indicate that r_{bp} does not depend on ϕ_{bp}. As outlined in *Methods* forward selection with competing model evaluation based on a lower AIC of at least 2 points was used to find the best fitting model. The final equation for r_{bp} as a function of θ_{bp} is:

$$r_{bp} = -0.4905\ \theta_{bp} + 36.489,\ R^2 = 0.834 \qquad (1),$$

where θ_{bp} is in degrees and r_{bp} is in millimeters. The 95% confidence intervals for the θ_{bp} coefficient and intercept are [-0.5236, -0.4574] and [35.8804, 37.0967], respectively. Note that Eqn 1 is only valid for the right side of the seal's face, where θ_{bp} varies between -90° (ventral) to +90° (dorsal). Results must be mirrored about the y-axis to produce results for the left side.

Table 1. Best fit equations for radial basepoint coordinate and angles of emergence by individual animal, along with combined equations across animals. Abbreviations: Prm: Parameter; (n): number of whiskers.

	Prm	Animal (n)	Coefficients				95% Confidence Intervals				Adj. R^2
			c_1	c_2	c_3		c_1	c_2	c_3		
1	r_{bp}	Seal 1 (56)	N/A	-0.42203	36.525		N/A	[-0.4729, -0.3711]	[35.5827, 37.4682]		0.833
		Seal 2 (62)	0.003283	-0.53157	35.899		[4.970e-04, 0.0060702]	[-0.5945, -0.4687]	[34.6273, 37.1707]		0.838
		Seal 3 (53)	0.004162	-0.61645	35.195		[0.001343, 0.006980]	[-0.6877, -0.5452]	[33.8951, 36.4957]		0.882
		Combined (171)	N/A	-0.4905	36.489		N/A	[-0.5236, -0.4574]	[35.8804, 37.0967]		0.846
		Final equation for radial basepoint coordinate: $r_{bp} = c_1\theta_{bp}^2 + c_2\theta_{bp} + c_3$, where r_{bp} is in millimeters and θ_{bp} is in degrees.									
			c_1	c_2	c_3	c_4	c_1	c_2	c_3	c_4	
2	θ_w	Seal 1 (56)	N/A	-0.972	1.815	133.02	N/A	[-1.1597, -0.7849]	[1.6454, 1.9849]	[129.9012, 136.1351]	0.903
		Seal 2 (62)	N/A	-1.141	1.647	138.42	N/A	[-1.3181, -0.9631]	[1.4731, 1.8199]	[135.3208, 141.5222]	0.889
		Seal 3 (53)	0.0504	-0.749	1.856	133.85	[0.0394, 0.0615]	[-0.9656, -0.5319]	[1.6882, 2.0236]	[129.8400, 137.8607]	0.923
		Combined (171)	N/A	-1.100	1.770	138.42	N/A	[-1.2346, -0.9655]	[1.6481, 1.8927]	[136.1603, 140.6733]	0.854
		Final equation for azimuthal angle of emergence: $\theta_w = c_1\phi_{bp}^2 + c_2\phi_{bp} + c_3\theta_{bp} + c_4$, where θ_w, ϕ_{bp} and θ_{bp} are in degrees.									
3	ϕ_w	Seal 1 (56)	N/A	1.700	N/A	-23.345	N/A	[1.5198, 1.8800]	N/A	[-26.3311, -20.3596]	0.867
		Seal 2 (62)	N/A	1.449	N/A	-21.738	N/A	[1.3460, 1.5526]	N/A	[-23.4949, -19.9809]	0.928
		Seal 3 (53)	0.0127	1.730	N/A	-19.799	[0.003515, 0.02179]	[1.5494, 1.9098]	N/A	[-22.9582, -16.6397]	0.882
		Combined (171)	N/A	1.570	N/A	-20.928	N/A	[1.4802, 1.6597]	N/A	[-22.3935, -19.4632]	0.875
		Final equation for elevation angle of emergence: $\phi_w = c_1\phi_{bp}^2 + c_2\phi_{bp} + c_3\theta_{bp} + c_4$, where ϕ_w, ϕ_{bp}, and θ_{bp} are in degrees.									
4	ζ_w	Seal 1 (56)	N/A	-1.350	1.573	-23.663	N/A	[-1.7195, -0.9803]	[1.2382, 1.9078]	[-29.8110, -17.5155]	0.693
		Seal 2 (62)	N/A	-1.565	1.753	-23.714	N/A	[-1.8397, -1.2893]	[1.4836, 2.0214]	[-28.5220, -18.9053]	0.818
		Seal 3 (53)	N/A	-1.732	2.308	-28.091	N/A	[-2.1166, -1.3482]	[1.9916, 2.6238]	[-34.2624, -21.9194]	0.840
		Combined (171)	N/A	-1.540	1.866	-24.447	N/A	[-1.7351, -1.3448]	[1.6882, 2.0429]	[-27.7197, -21.1746]	0.784
		Final equation for twist angle of emergence: $\zeta_w = c_1\phi_{bp}^2 + c_2\phi_{bp} + c_3\theta_{bp} + c_4$, where ζ_w, ϕ_{bp}, and θ_{bp} are in degrees.									

Eqn 1 indicates that r_{bp} decreases from caudal to rostral. This trend is depicted in Fig. 4C and is primarily caused by the orientation of the seal's mystacial pad. The pad is nearly vertical in the dorsoventral direction, so ϕ_{bp} does not contribute to changes in r_{bp}. In contrast, the mystacial pad varies considerably in the mediolateral direction, so r_{bp} varies systematically with θ_{bp}.

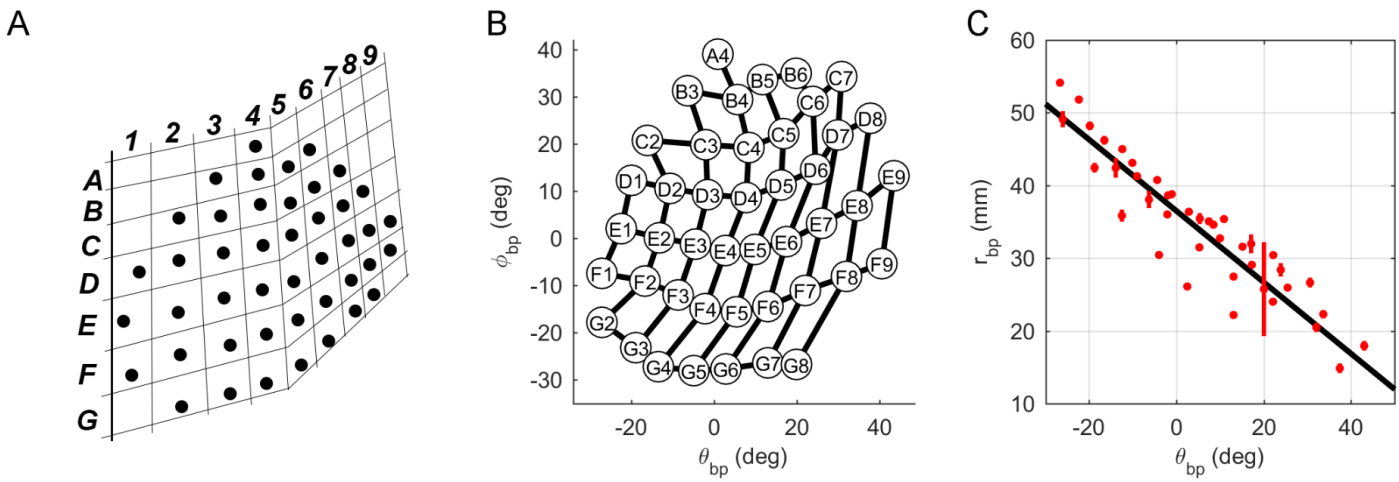

Fig. 4: Locations of whisker basepoints are described in spherical coordinates (r_{bp}, θ_{bp}, ϕ_{bp}). (A) Qualitative description of the shape of the harbor seal whisker array from previous studies. Figure is recreated from Dehnhardt and Kaminski, 1995. **(B)** Plotting ϕ_{bp} against θ_{bp} quantifies the geometry of the array in a manner that closely resembles the qualitative description in (A). **(C)** Radial basepoint coordinate (r_{bp}) is plotted as a function of θ_{bp}. Black line represents Eqn 1. The mean of r_{bp} when grouped by Row and Column identity is represented by the red dots; red vertical bars indicate standard errors.

3.4 Two-dimensional shape: arclength and curvature

We used the basepoint coordinates θ_{bp} and ϕ_{bp} as independent variables to quantify variations in arclength (S) and intrinsic whisker curvature (A) across the array. To provide visual intuition for S and A, traces of the F-row of whiskers from a single seal (Seal 1) are shown in black in Fig. 5A. In general, the whiskers decrease in length and increase slightly in intrinsic curvature from caudal to rostral, but there is considerable variability, especially for whiskers F4 and F5. A sense for the magnitude of the variability is provided in the red traces of Fig. 5A, which show whiskers F4 and F5 obtained from the two other seals.

When averaged across all animals, whisker arclength is best described as an exponential function of θ_{bp} and ϕ_{bp}.

$$S = \exp(-0.0321\,\theta_{bp} - 0.0114\,\phi_{bp} + 3.764) \qquad \text{Adj. } R^2\text{: } 0.735 \qquad (2)$$

where θ_{bp} and ϕ_{bp} are in degrees and S is in millimeters. The 95% confidence intervals for the θ_{bp}, ϕ_{bp} coefficients and intercept are [-0.0388, -0.0254], [-0.0155, -0.00728], and [3.6861, 3.8422], respectively. As for Eqn 1, Eqn 2 only holds for the right side, where θ_{bp} varies from -90° (caudal) to +90° (rostral) and ϕ_{bp} varies from -90° (ventral) to +90° (dorsal). Recall also that this fit was found using only the 2D data (44 whiskers) because the 3D laser scanner truncated the distal portions of the whiskers during the 3D scans.

Notice that Eqn 2 has negative coefficients in front of both θ_{bp} and ϕ_{bp}, confirming the visual impression from Fig. 5A that whiskers tend to decrease in length from caudal to rostral, and also indicating that whisker length tends to decrease from ventral to dorsal. The dependence on ϕ_{bp} is considerably weaker than the dependence on θ_{bp}, so that a change in the value of θ_{bp} will cause the arclength to change considerably more than the equivalent change in ϕ_{bp}.

The exponential decrease of S with increases in θ_{bp} and ϕ_{bp} is shown in Fig. 5B, where the surface represents Eqn 2 and the red points are the mean value of S when grouped by whisker identity +/- the standard error. The surface shown in Fig. 5B is more intuitively represented by an alternative form of Eqn 2:

$$S = \frac{43.12}{\left(e^{0.0321\theta_{bp} + 0.0114\varphi_{bp}}\right)} \qquad \text{Adj. } R^2\text{: } 0.74 \qquad (3)$$

Eqn 3 indicates that S will equal ~43 mm in the middle of the array, where both θ_{bp} and ϕ_{bp} equal zero, and then vary exponentially in both directions from that central point.

Fig. 5C compares the arclength values predicted by Eqns 2 and 3 with the raw measurements. A perfect model of the data would lie along the diagonal line. Instead, the model underestimates the length of whiskers longer than ~60 mm, and whiskers shorter than ~60 mm are clustered with a relatively broad distribution about the diagonal. It seems likely that the prediction for arclength could be significantly improved with more data. Finally, Fig. 5D shows predicted values for S across the whisker array, confirming that the caudal and ventral-most whiskers are the longest.

We next quantified intrinsic whisker curvature, using the same 44 whiskers used to quantify 2D arclength. The shapes of the seal's whiskers were found to be well described by the function $y = Ax^3$, with the coefficient A termed the "cubic curvature coefficient." When quantified in terms of basepoint parameters the value of A was not significant in ϕ_{bp}, so Eqn 4 expresses A only as a function of θ_{bp}:

$$A = 9.2327e^{-06}\,\theta_{bp} + 0.00022015 \qquad R^2\text{: } 0.667 \qquad (4)$$

In Eqn 4, θ_{bp} has units of degrees and A has units of $1/mm^2$.

However, further investigation found that whisker curvature was significantly better described as an exponential function of arclength rather than as a linear function of θ_{bp}, as seen in Eqn 5:

$$A = \exp(-0.030799\,S - 7.2348) \qquad R^2\text{: } 0.837 \qquad (5)$$

In Eqn 5, S has units of millimeters, and A has units of $1/mm^2$. The 95% confidence intervals for the arclength coefficient and intercept are [-0.0350, -0.0266] and [-7.4968, -6.9727], respectively. Consistent with the visual intuition provided in Fig. 5A, Eqns 4 and 5 indicate that shorter, more rostral whiskers typically have a higher curvature coefficient than the longer, more caudal whiskers.

Fig. 5E shows Eqn 5 as a solid black line plotted over the raw data points. Although the fit is excellent for whiskers with arclengths greater than ~55 mm, as indicated by the tight scatter of the points about the fit line, there is considerably more scatter about the curve for shorter whiskers. This increased scatter is easily observed when the experimental values for A are compared with those predicted by Eqn 5, as in Fig. 5F. These results closely resemble those found for rats and mice, whose short whiskers also exhibit high variability in intrinsic curvature (Belli et al., 2018; Bresee et al., 2023; Towal et al., 2011). Following the approach used for the rodents, we found the upper bound on the relationship between the curvature coefficient and arclength. This bound is shown as a thin, dashed, gray line in Fig. 5E, and is given by the equation:

$$A = 0.00100*\exp(-0.0296\,S) - 0.00000544 \qquad (6)$$

The upper bound limits the y-coordinate of the whisker's tip, perhaps reflecting a limit on the total "height" of the whisker (Belli et al., 2018). Note that for short whiskers, even a tiny change in the location of the whisker tip has a large effect on the curvature coefficient. In contrast, a small change in the location of the tip of a long whisker has only a small effect on the curvature coefficient.

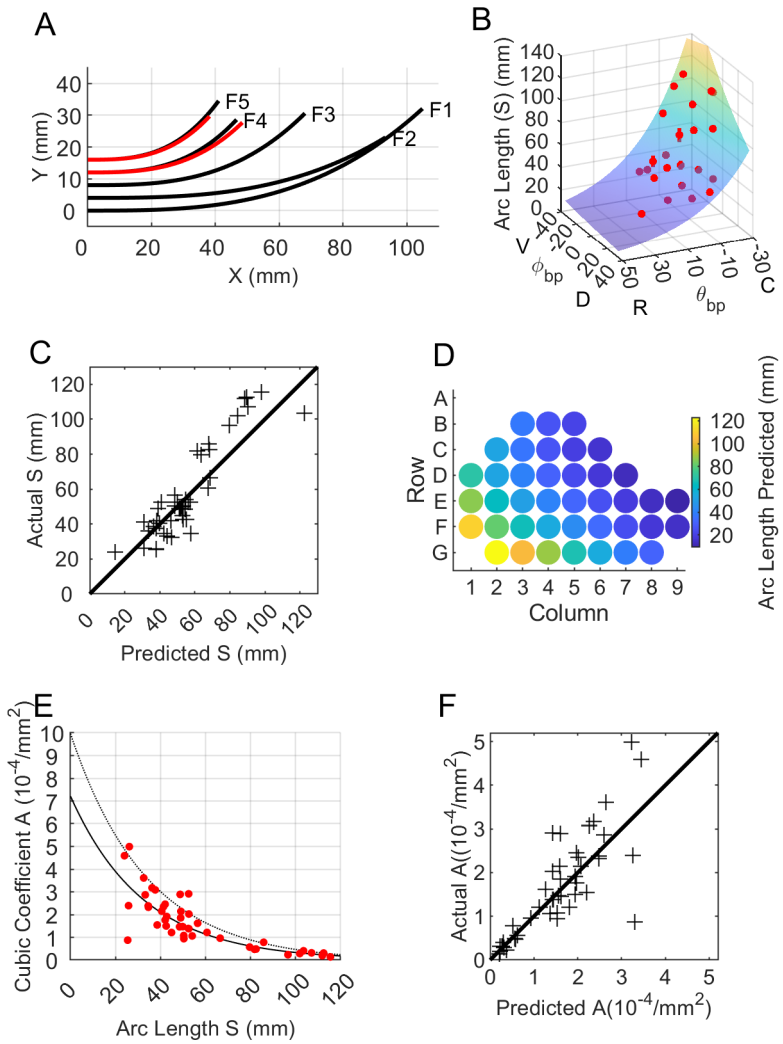

Fig. 5. Relationship between 2D whisker geometry and basepoint coordinates θ_{bp} and ϕ_{bp}. Panels B, C, E, and F show data for N = 44 seal whiskers scanned in 2D. **(A)** Black traces show the shapes of the F-row of whiskers from a single seal. Whiskers F4 and F5 from two other seals are shown in red to illustrate typical variability in arclength and curvature. **(B)** This subplot shows the surface described by Eqn 2. Arclength can be described as a decaying exponential function of the basepoint coordinates (θ_{bp} and ϕ_{bp}, both with units of deg) from caudal (C) to rostral (R) and ventral (V) to dorsal (D) across the array. Mean ± standard error when grouped by whisker identity is shown in red. **(C)** Experimentally measured values for arclength (S) are compared with values predicted from Eqn 2. Black diagonal line indicates equality. **(D)** A colormap shows how Eqn 2 predicted arclengths will vary across the array. **(E)** The cubic curvature coefficient (*A*) can be described as an exponentially decreasing function of arclength. The solid black line represents Eqn 5 and the dashed gray line represents Eqn 6. **(F)** Experimentally measured values for the curvature coefficient are compared with values predicted from Eqn 5. Black diagonal line indicates equality. Notice that the prediction quality decreases as *A* increases.

3.5 Angles of emergence of the whiskers on the mystacial pad

Finally, we used the basepoint coordinates θ_{bp} and ϕ_{bp} as independent variables to quantify the angles of emergence of the whiskers across the array. As shown in lines 2 - 5 of Table 1, the best fit equations for θ_w and ζ_w were linear in both θ_{bp} and ϕ_{bp}, while the best fit equation for ϕ_w depended only on ϕ_{bp}. The final equations for the angles of emergence were:

$$\theta_w = 1.770\,\theta_{bp} - 1.100\,\phi_{bp} + 138.42 \qquad \text{Adj. } R^2\text{: } 0.854 \qquad (7)$$

$$\phi_w = 1.570\,\phi_{bp} - 20.928 \qquad \text{Adj. } R^2\text{: } 0.875 \qquad (8)$$

$$\zeta_w = 1.866\ \theta_{bp} - 1.540\ \phi_{bp} - 24.447 \qquad \text{Adj. } R^2\text{: } 0.784 \qquad (9)$$

In Eqns 7, 8, and 9, all variables have units of degrees.

Fig. 6 compares these equations with experimentally-measured values. The horizontal emergence angle (θ_w) increases from caudal to rostral across the array and decreases from ventral to dorsal (Fig. 6A). The elevation angle ϕ_w increases from ventral to dorsal, with no significant change in the caudal-rostral direction (Fig. 6B). Notably, the ϕ_w angles are not symmetric about 0 deg, indicating that the whiskers are skewed to point downward. The twist angle, ζ_w, increases from caudal to rostral across the array and decreases from ventral to dorsal (Fig. 6C).

The subplots of Figs. 6DEF show that actual vs. predicted values for each angle of emergence are relatively uniformly dispersed about the equality line, thus confirming that the models shown in Figs. 6ABC were correctly chosen.

Visual intuition for the overall orientation of whiskers on the pad is provided in Figs. 6GHI. Most rostral whiskers emerge from the face pointing forwards and towards the midline, while most caudal whiskers emerge pointing slightly backwards (Fig. 6G). Dorsal whiskers emerge pointing upwards; ventral whiskers downwards (Fig. 6H). Whiskers in the dorsal-caudal regions of the array are oriented the most concave backwards, and rostral-ventral whiskers the most concave forwards (Fig. 6I). Finally, the pattern of variation for ζ_w is strikingly similar to that of θ_w; in fact, these two variables are closely linear with r = 0.875 (Pearson correlation).

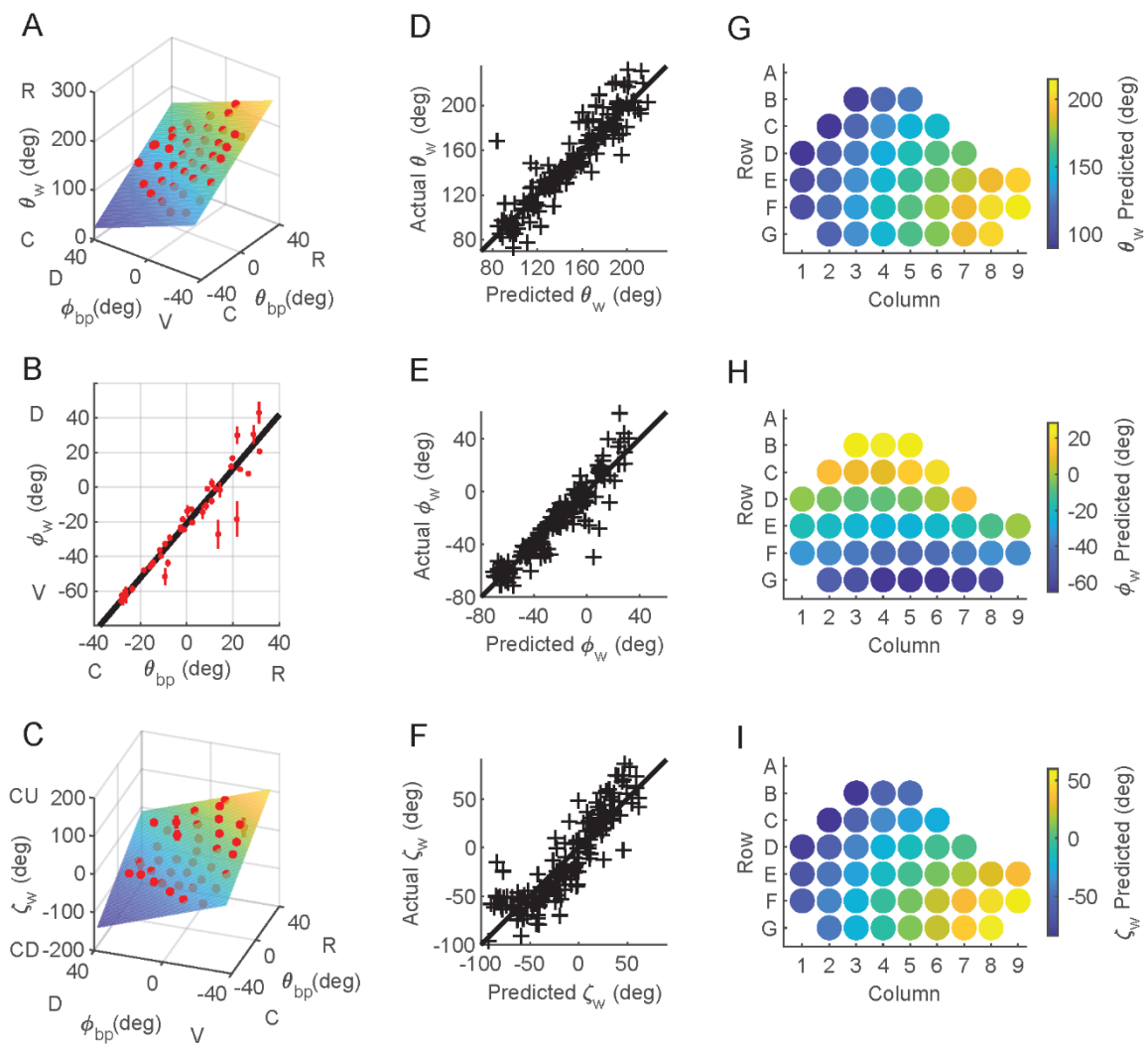

Fig. 6: Relationship between whisker angles of emergence and basepoint coordinates. Panels A – F show data for N = 171 seal whiskers identified in Table 1. **(ABC)** The subplots show the horizontal angle of emergence

(θ_w) fit to Eqn 7, the elevation angle of emergence (ϕ_w) fit to Eqn 8, and the twist angle of emergence (ζ_w) fit to Eqn 9. For all plots, the mean ± standard error when grouped by whisker identity is shown in red. Abbreviations: C: caudal; R: rostral; D: dorsal; V: ventral; CU: concave up; CD: concave down. **(DEF)** The subplots show actual values of θ_w, ϕ_{bp}, and ζ_w compared with values predicted from Eqns 7, 8, and 9. All subplots reveal relatively uniform dispertion of actual vs. predicted values about the line y = x, indicating that the correct model was selected. **(GHI)** The subplots show how values for θ_w, ϕ_{bp}, and ζ_w are predicted to vary across the array using Eqns 7, 8, and 9. θ_w, ϕ_{bp}, and ζ_w have units of deg.

3.6 Equations used to generate a CAD model of the harbor seal whisker array

Together, the equations of previous sections can be used to generate a full 3D model of the harbor seal vibrissal array. Fig. 7 shows 3D CAD models of the array imposed on 3D scans of seal heads. The model in Fig. 7A was created using portions of the 3D point clouds that were previously discarded from a scan of Seal 1, and can be compared with the photographs of Seal 2 shown in Fig. 7B. The model is symmetric about the midsagittal plane and has been smoothed extensively. The model of the seal head in Fig. 7C is higher resolution, contains all facial features, and is asymmetric about the midsagittal plane; this scan was obtained from a deceased seal in a separate experiment. Comparing the models with the photographs provides visual intuition for the model's descriptive ability.

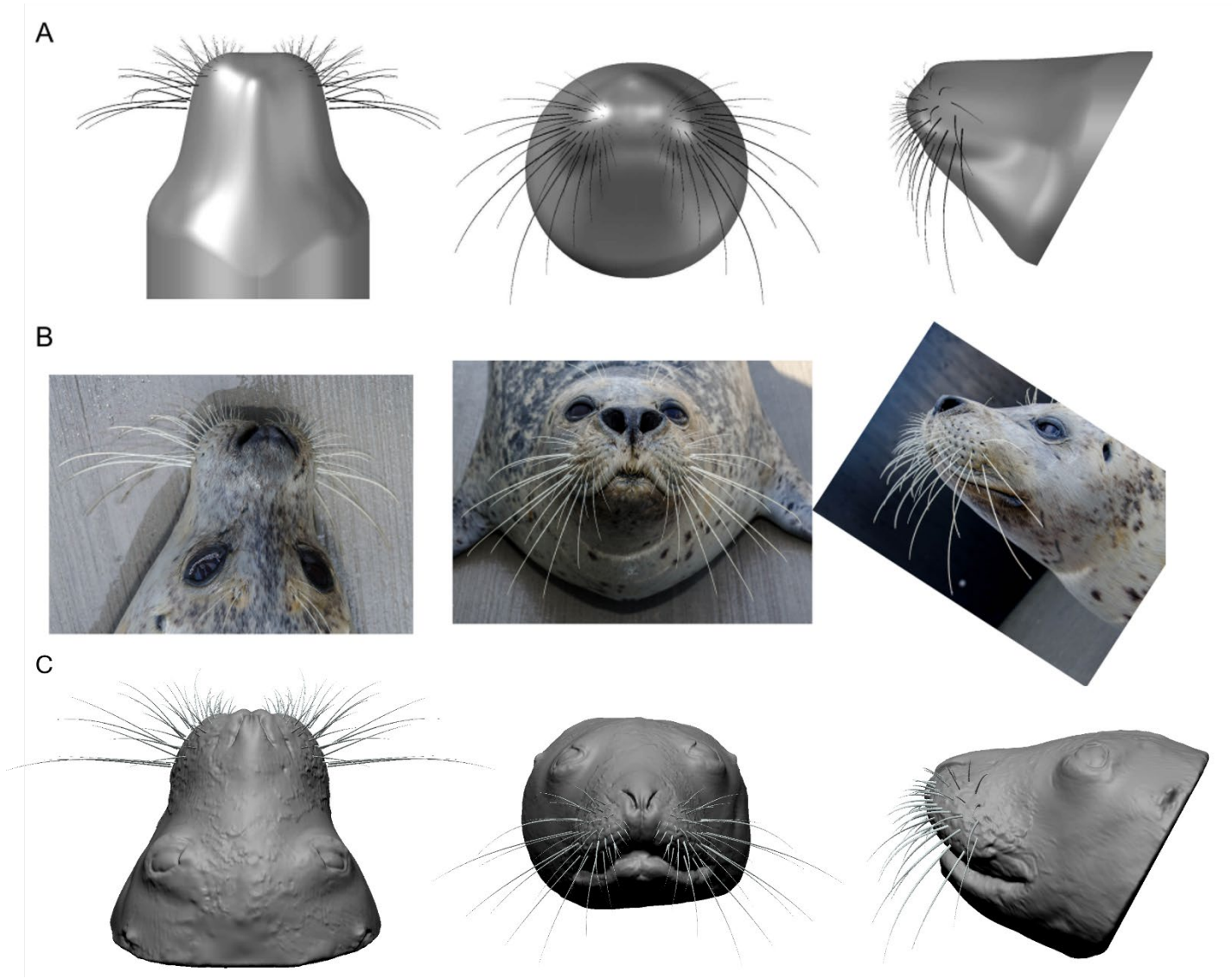

Fig. 7: The model of the seal whisker array is compared with photographs.

3.7 Comparing the vibrissal arrays of harbor seals, mice, and rats

Equations for seals, rats, and mice are compared in Table 2 and visualized in Fig. 8. When the 3D models are overlaid (Fig. 8A) the most obvious difference is size. The entire rat whisker array fits within the bounds of the seal's basepoints. A side-view of the basepoints of the three species (Fig. 8B) provides additional visual intuition: the entire mouse basepoint array could fit between two caudal seal basepoints.

Overall size and shape differences are also revealed by plotting r_{bp} as a function of θ_{bp} and ϕ_{bp} (Table 2, line 1). These plots (Fig. 8C) show that values of r_{bp} for the seal are much larger than those for rats and mice, again demonstrating the size difference. The planes also show that r_{bp} for the seal changes much more steeply with θ_{bp}, indicating that the seal's whisker basepoints are located more rostrally than are those of the two rodents.

Although Figs. 8ABC show that seal whiskers are spaced further apart than rodent whiskers in linear distance, this spacing could simply be a result of head size. To normalize for head size, we analyzed the angular spacing of basepoints across species. Fig. 8D shows whisker basepoint locations when plotted as functions of ϕ_{bp} and θ_{bp} for the rat, mouse, and seal. Within these angular coordinates mice and rats have approximately the same number of whiskers, but the seal has far more whiskers, more densely packed.

Turning from whisker basepoint location to 2D whisker geometry, Line 2 of Table 2 indicates that seal whisker arclength depends on both rostrocaudal and dorsoventral position (θ_{bp} and ϕ_{bp}), while for rodents it depends only on rostrocaudal position (θ_{bp}). These differences are visualized in Fig. 8E; note that the longest seal whisker is only ~2 times longer than the longest rat whisker. Because seal whiskers were parameterized by cubic functions while rodent whiskers were fit to quadratics, their shapes cannot be directly compared in the present work (but see Luo and Hartmann, 2023). However, an overlay of all individual whisker fits provides visual intuition for the similarity of whisker curvature for mice and rats (Fig. 8F), and differences in whisker curvature of the seal (Fig. 8G).

Finally, Figs. 8HIJ visualize the equations in lines 5, 6, and 7 of Table 2. The values of the horizontal angle (θ_w) depend on both θ_{bp} and ϕ_{bp} for seals and rats, but only on θ_{bp} for the mouse. They are generally larger in seals than in rodents (Fig. 8G). Thus not only are the seal's whisker basepoints located more rostrally, but the whiskers emerge at angles that point more rostrally than on rodents. For all three species the elevation angle (ϕ_w) depends only on θ_{bp}. The relationship between ϕ_w and θ_{bp} for the seal has a significantly steeper slope and is offset towards negative values, indicating that whiskers emerge from the seal's face pointing more ventrally than on mice or rats (Fig. 8H). Finally, for all species the whisker twist angle (ζ_w) depends on both θ_{bp} and ϕ_{bp}, but the equations are quite different between the seal and the two rodents. Visualizing the equations (Fig. 8I) shows that seal whiskers span a much larger range of values of ζ_w than rodent whiskers. In addition, ζ_w deceases with elevation angle for the seal, while it increases with elevation angle for both rats and mice.

Table 2. Equations describing the morphology of the harbor seal vibrissal array compared with equations describing the morphology of rats and mice. Rat data are from Belli et al., 2018. Mouse data are from Bresee et al., 2023. All angles are in degrees and r_{bp} and S are in mm. The upper bound on curvature (A) has units of 1/mm for mouse and rat, and 1/mm^2 for the seal.

Parameter	Species	Equation	Equation no. in text	R^2 value
1 Radial basepoint	Mouse	$r_{bp} = -0.0152\ \theta_{bp} - 0.0165\ \phi_{bp} + 4.44$		Adj. $R^2 = 0.55$
	Rat	$r_{bp} = -0.0265\ \theta_{bp} - 0.0160\ \phi_{bp} + 6.85$ (forced to linear)		Adj. $R^2 = 0.55$
		$r_{bp} = -0.0295\ \theta_{bp} - 0.0162\ \phi_{bp} + 6.50 + 0.000511\ \theta_{bp}^2$		Adj. $R^2 = 0.65$
	Seal	$r_{bp} = -0.4905\ \theta_{bp} + 36.489$:	Eqn 1	$R^2 = 0.83$
2 Arclength	Mouse	$S = \exp(-0.0184\ \theta_{bp} + 2.46)$		$R^2 = 0.67$
	Rat	$S = \exp(-0.0246\ \theta_{bp} + 3.12)$		$R^2 = 0.85$
	Seal	$S = \exp(-0.0321\ \theta_{bp} - 0.0114\ \phi_{bp} + 3.764)$	Eqn 2	Adj. $R^2 = 0.74$
3 Upper bound on intrinsic curvature	Mouse	$y = Ax^2$, $A = 0.294 \exp(-0.262\ S) + 0.012$		
	Rat	$y = Ax^2$, $A = 0.0746 \exp(-0.0506\ S) + 0.00479$		
	Seal	$y = Ax^3$, $A = 0.00100*\exp(-0.0296\ S) – 0.00000544$	Eqn 6	
4 Horizontal emergence angle	Mouse	$\theta_w = 0.922\ \theta_{bp} + 85.1$ (Row A removed)		$R^2 = 0.74$
	Rat	$\theta_w = 0.680\ \theta_{bp} + 67.24$ (forced to one predictor)		$R^2 = 0.52$
		$\theta_w = 0.598\ \theta_{bp} – 0.314\ \phi_{bp} + 67.4$		Adj. $R^2 = 0.64$
	Seal	$\theta_w = 1.770\ \theta_{bp} – 1.100\ \phi_{bp} + 138.42$	Eqn 7	Adj. R^2: 0.854
5 Elevation emergence angle	Mouse	$\phi_w = 1.00\ \phi_{bp} + 10.2$		$R^2 = 0.76$
	Rat	$\phi_w = 1.04\ \phi_{bp} + 6.68$		$R^2 = 0.85$
	Seal	$\phi_w = 1.570\ \phi_{bp} – 20.928$	Eqn 8	Adj. R^2: 0.875
6 Twist emergence angle	Mouse	$\zeta_w = 0.620\ \theta_{bp} + 1.00\ \phi_{bp} + 43.0$ (Row A removed)		Adj. $R^2 = 0.34$
	Rat	$\zeta_w = 0.876\ \theta_{bp} + 0.845\ \phi_{bp} + 37.9$		Adj. $R^2 = 0.42$
	Seal	$\zeta_w = 1.866\ \theta_{bp} – 1.540\ \phi_{bp} – 24.447$	Eqn 9	Adj. R^2: 0.784

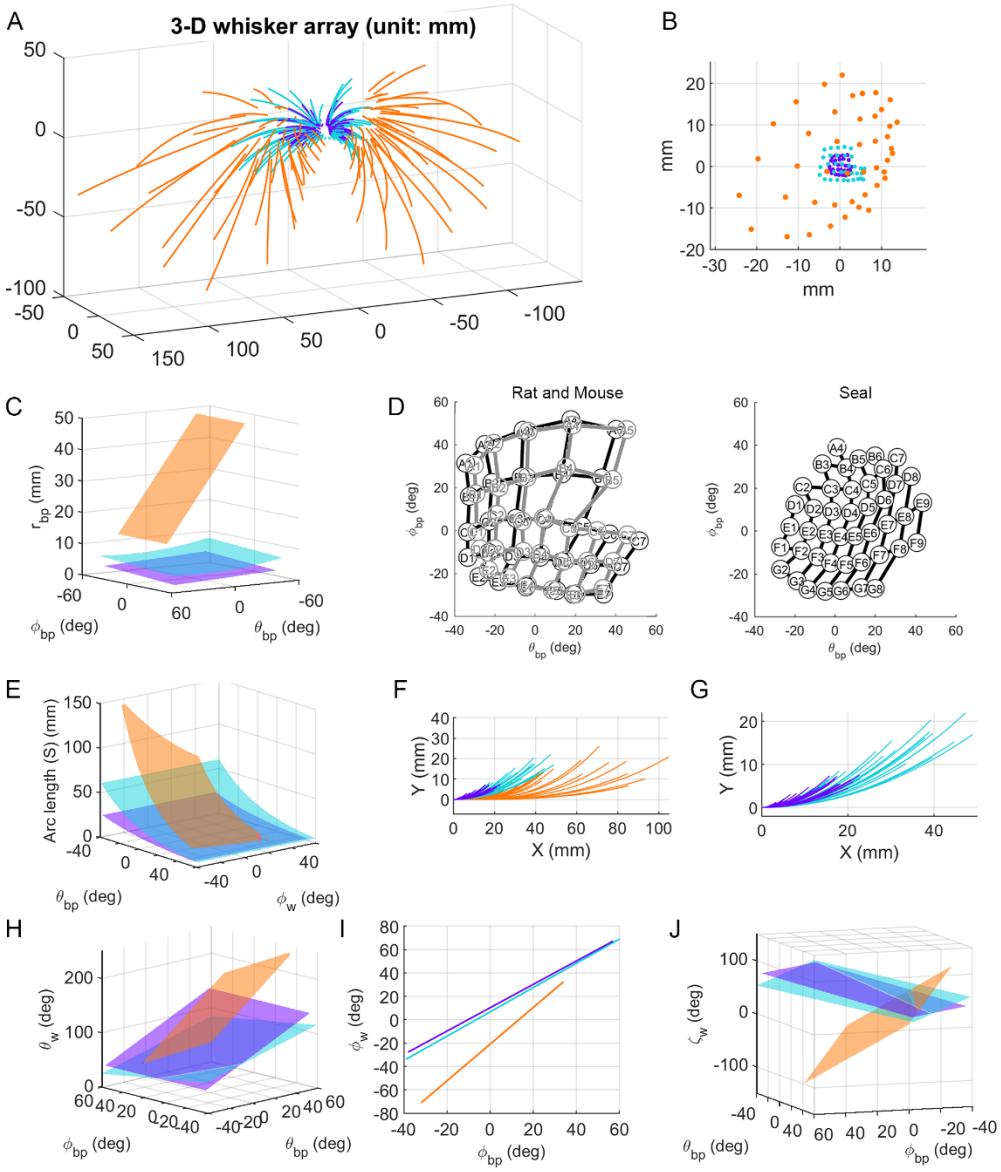

Fig. 8. The harbor seal whisker array is compared to arrays of rats and mice. In all panels the data for harbor seals are in orange, rats in teal, and mice in purple. **(A)** Full 3D geometric models of seal, rat, and mouse whisker arrays are shown in standard position and orientation. Rat data are from Belli et al., 2018. Mouse data are from Bresee et al., 2023**. (B)** Whisker basepoints are plotted in the sagittal (y-z) plane. **(C)** Plotting r_{bp} as a function of basepoint position (Table 2, line 1) highlights the large size differences between species. **(D)** To normalize for head size, mean whisker basepoint locations for all three species are plotted in θ_{bp} and ϕ_{bp}. In these angular coordinates, seal whisker basepoints (right panel) are spaced more densely than mouse and rat whisker basepoints (overlayed in the left panel). Mouse data from Bresee et al., 2023. Rat data from Belli et al., 2018. The right panel shows the same data as Fig. 4D of the present work. **(E)** Whisker arclength (S) is plotted as a function of basepoint position (θ_{bp} and ϕ_{bp}). **(F)** Seal whiskers are fit with cubic equations, while **(G)** mouse and rat whiskers are fit with quadratic equations. The inset shows the large overlap in mouse and rat whisker shapes. The proximal portion of all whiskers is aligned with the x-axis. **(H,I,J)** Rostral-caudal emergence angle (θ_w), elevation emergence angle (ϕ_w), and twist emergence angle are plotted as functions of basepoint position (θ_{bp} and ϕ_{bp}).

4. Discussion

4.1. A head-centered approach to quantifying whisker morphology across species

An important contribution of the present work is the demonstration of a quantitative approach to compare whisker array morphology across species, regardless of whisker number and arrangement. Standard morphometric techniques cannot be used to compare whisker arrays because they rely on matching landmarks or semi-landmarks (Bookstein, 2018; Shui et al., 2023). Given that different animal species have very different whisker numbers and arrangements, and that whiskers evolved independently multiple times (Muchlinski, 2006; Muchlinski, 2010a; Muchlinski, 2010b; Muchlinski et al., 2020), finding whisker-based correspondences is not generally possible.

To address this problem our laboratory developed a head-centered approach for cross-species comparisons of whisker arrays. This approach was first proposed in Belli et al., 2018, and first used in a study that compared the morphology of mouse and rat vibrissal arrays (Bresee et al., 2023). However, the 2023 study did not fully highlight the power of the approach because mice and rats have very similar whisker numbers and arrangements – in principle, their arrays could have been compared using row and column whisker identities.

The present study uses the head-centered approach to compare the whisker arrays of harbor seals, which have ~50 mystacial whiskers arranged in seven rows, with the arrays of mice and rats, which have ~30 mystacial whiskers arranged in five rows. Even though it is not possible to identify "corresponding" whiskers between the animals, equations for whisker array geometry can be quantitatively compared (Table 2). Because basepoint coordinates do not rely on a row and column arrangement, the approach could even be extended to animals with "disorganized" whisker arrays, such as pigs (Muchlinski et al., 2020).

4.2. Remarks on the head-centered approach

(1) Choices for the origin and horizontal plane are extremely important – these choices affect all basepoint coordinates, and thus all equations. Different choices may yield more (or less) parsimonious equations. We anticipate that examining how equations change depending on these choices will be a rich area for future study, particularly in the context of multimodal sensory integration.

(2) The present work used the whisker basepoints (θ_{bp} and ϕ_{bp}) as independent variables to develop equations for whisker arclength, curvature coefficient, and angles of emergence. Similar equations could be developed for other aspects of whisker geometry. For example, harbor seal whiskers have ellipsoidal cross-sections and undulations along their length (Ginter et al., 2012; Ginter et al., 2010; Murphy et al., 2013; Summarell et al., 2015). Equations based on θ_{bp} and ϕ_{bp} could be written for major and minor diameter axes, as well as for undulation angles.

(3) The head-centered approach for comparing whisker geometry across species complements previous work that has correlated whisking behavior with whisker musculature, skull features, activity patterns (diurnal, cathemeral, or nocturnal), and substrate preference (arboreal, terrestrial, or marine) (Muchlinski et al., 2020). A notable advantage of correlating skull morphometrics with whisking behavior is that the analyses can be applied to extinct species, particularly useful for evolutionary studies (Muchlinski, 2010a).

(4) Applying the head-centered approach to local regions of a whisker array may help reveal mystacial pad functional compartmentalization. For example, rostral-caudal or dorsoventral compartmentalization could be indicated if these regions of the array were found to be best described by two different sets of equations. These predictions could then be tested with behavioral observation and analysis of musculature.

(5) Models of animal bodies, head, faces, and whisker arrays are increasingly used in simulations of animal sensorimotor behaviors (Bolaños et al., 2021; Zweifel et al., 2021). However, equation-based models will not represent whisker array geometry as accurately as models that simply average the array across individuals of the same species. When available, we strongly recommend using "average" models instead of "equation based" models for behavioral and neurophysiological simulations.

4.3. Whisker basepoint positions on the face reflect both head size and shape

The mystacial pad of the seal is much larger than that of rats and mice, and whiskers are spaced further apart in linear distance (Figs. 8AB). The equation for the radial basepoint is offset by 36 mm for the seal, ~8 times the offset for mice, and ~5 times the offset for rats (Table 2, Line 1; Fig. 8C). After normalizing for head size, however, seal whisker basepoints have a denser angular spacing than the basepoints of either rodent (Fig. 8D).

Whisker basepoint positions also reflect head shape. Seal whisker basepoints are located more rostrally and more ventrally than on mice and rats. For both mouse and rat, r_{bp} decreases with both θ_{bp} and ϕ_{bp}. In contrast, in the seal, r_{bp} decreases with θ_{bp} but does not vary with ϕ_{bp}, indicating that whiskers are positioned on the snout at locations with approximately constant dorsoventral curvature.

4.4. Arclength decreases exponentially across the whisker array and correlates poorly with body size

Consistent with previous studies of mice and rats (Brecht et al., 1997; Pocock, 1914; Towal et al., 2011), we find that seal whisker arclength increases exponentially from rostral to caudal but also increases significantly from dorsal to ventral (Table 2, line 2). The range of whisker arclength is larger for rats than mice, and larger still for seals, as shown in Fig. 8E and reflected by the steeper exponential decay (Table 2, line 2).

Intriguingly, whisker length is poorly correlated with body size. Seals are ~375 times the weight of a rat and ~3,750 times the weight of a mouse (Burns, 2009). However, the longest seal whiskers are only ~2x the longest rat whiskers and ~4x the longest mouse whiskers (Figs. 8EG). Nearly all mouse whiskers have arclengths between 10 – 30 mm, and nearly all rat and seal whiskers have arclengths between 10 and 60 mm. The extensive overlap in these size ranges is striking, indicating a restricted range of useful whisker lengths across body size.

4.5. Variations in intrinsic whisker curvature across the array

The present work measured the intrinsic curvature of seal whiskers when they were hydrated. Many different methods have been used to quantify the intrinsic curvature of animal whiskers, and these methods are comprehensively reviewed, compared, and contrasted in Luo and Hartmann, 2023. The present work uses single-parameter polynomial fits as intuitive descriptions of whisker shape: rat and mouse whiskers are best fit by quadratics (Belli et al., 2018; Bresee et al., 2023; Knutsen et al., 2008; Towal et al., 2011), while seal whiskers are best fit by cubics (Figs. 5E, 8F). This shape difference could reflect adaptation to a hydrodynamic environment, differences in predation, or the larger evolutionary separation between phocines and rodents. Like rat and mouse whiskers (Belli et al., 2018; Bresee et al., 2023; Knutsen et al., 2008; Towal et al., 2011), longer seal whiskers tend to be straighter than shorter whiskers and the shortest whiskers exhibit the largest variability in curvature coefficient (Figs. 5EF).

4.6. The orientation of a seal whisker on the head: "curvature orientation" is different from "diameter orientation"

The whiskers of many marine mammals have elliptical cross-sections, and studies have often defined the "orientation" of the whisker based on which side of the whisker has the larger diameter (Ginter et al., 2010; Miersch et al., 2011; Murphy et al., 2013). In contrast, whiskers of terrestrial mammals tend to have circular cross sections, and studies have defined whisker "orientation" based on the whisker's intrinsic curvature (Belli et al., 2018; Bresee et al., 2023; Knutsen et al., 2008; Petersen et al., 2021; Quist and Hartmann, 2012). It is, therefore, critical to keep "curvature-orientation" distinct from "diameter-orientation," as these two different geometric features will have independent effects on the whisker's mechanical response to flow.

Although the present work did not directly measure diameter orientation, Summarell et al., 2015, found that the intrinsic curvature of a harbor seal whisker aligns with its major axis (larger diameter) and that the flexural stiffness along the major axis is nearly double that of the minor axis. The orientation of the major axis (and greatest stiffness) will thus correlate with the twist angle (ζ_w) as shown in Figs. 6CFI.

4.7. Comparing emergence angles across species

As discussed in *Methods*, emergence angles (θ_w, ϕ_w, ζ_w) for the seal were measured with the whiskers in a neutrally relaxed position. Future work could simulate and quantify the angles associated with whisker array motion; here we assess the neutral, relaxed emergence angles presented in *Results*.

Not only are whisker basepoints more rostral and more ventral on seals than on rats and mice, but seal whiskers emerge from the face pointing more forwards and downwards than the whiskers of rats and mice. This orientation places the tips of the seal's whiskers closer to its mouth, potentially advantageous during prey capture (Dehnhardt and Kaminski, 1995). Seals may not need ventrally-located whiskers because they often swim upside-down, allowing the animal to visually scan the environment below while using vibrissae to sense the environment above.

An important similarity between the whisker arrays of mice, rats, and seals is the strong, single-variable linear relationship between elevation angle (ϕ_w) and the dorso-ventral location of the whisker basepoint (ϕ_{bp}), indicating that ϕ_w is constant within a row (Fig. 8H; Table 2, Line 5). This similarity is striking given that their last common ancestor is estimated to have lived between ~90 and ~65 MYA (Meredith et al., 2011; O'Leary et al., 2013). For a qualitative sense for the state of the mammalian clade in this era, consider that the last common ancestor of seals, mice, and rats lived before the divergence of the ancestral *Laurasiatherian* (the ancestor of modern animals as diverse as carnivores, ungulates, bats, cetaceans, and shrews) and the ancestral *Euarchontoglire* (the ancestor of all rodents, lagomorphs, and primates).

A possible advantage of a linear relationship between ϕ_w and ϕ_{bp} is that it could simplify the calculation of elevation angle during sequential whisker contacts. A stimulus moving from rostral to caudal through a row of whiskers at rest will make sequential contact with the whiskers in that row. To combine information across whiskers and determine 3D stimulus location, the animal's nervous system must keep track of the azimuthal angle (θ_w) of each whisker separately, but the elevation angle will remain constant. This computational advantage applies even to mobile whiskers, provided there is a fixed relationship between protraction and elevation and between protraction and roll. Such fixed relationships have already been observed for rats and mice (Knutsen et al., 2008; Petersen et al., 2021), and whisker movements of other species may exhibit similarly fixed relationships. Future work should examine the extent to which the single-variable, linear relationship between ϕ_w and ϕ_{bp} generalizes across species.

A second similarity across all three species is that the twist of the whisker about its own axis (ζ_w) varies in a smooth, diagonal gradient across the array. This orientation gradient could be particularly useful for determining the direction of a stimulus moving across the array. Stimuli interacting with many stationary whiskers at once, such as air or water flow, will encounter different gradients of whisker twist for any pitch of the animal's head. Stimulus direction could be inferred from these gradients because the mechanical response of each whisker will depend strongly on its orientation relative to the stimulus (Quist and Hartmann, 2012; Yu et al., 2016b).

In the seal, the angle ζ_w varies between ~-90 and ~60 degrees, so more caudal whiskers are oriented concave backwards, while more rostral whiskers are oriented concave down. In contrast, rat and mouse whisker arrays have many whiskers oriented concave forwards (Belli et al., 2018; Knutsen et al., 2008; Quist and Hartmann, 2012; Towal et al., 2011). These orientations make sense – pushing a concave-forward whisker through water would cause turbulence and complicate sensing. In contrast, rotating a concave-forward whisker through air would extend tactile reach.

4.8. Wake detection and whisker mechanical responses

Harbor seals use their whiskers to track the wakes of fish (Dehnhardt et al., 1998; Dehnhardt et al., 2001; Wieskotten et al., 2010; Wieskotten et al., 2011). To understand the mechanics underlying this complex behavior requires analysis of (1) the 3D geometry of individual seal whiskers and their 3D arrangement on the face, as quantified in the present work, (2) fluid-structure interactions between (moving and deforming) seal whiskers, head, and body, and (3) externally-generated wake structure and flow profiles.

The mechanical response of a seal whisker to a given stimulus will depend on its arclength and curvature, the taper of its elliptical cross-section diameter, the 3D geometry of undulations along its arclength, its hydration state, and material anisotropies. The whisker's natural frequencies will be closely related to the ratio of its base diameter to the square of its arclength (D/S^2) (Georgian, 1965), so it is immediately apparent that – as for the rat (Boubenec et al., 2012; Hartmann et al., 2003; Neimark et al., 2003; Ritt et al., 2008) – the regular arrangement of long and short whiskers (Fig. 5) will create a mechanical filter across the array (Hanke et al., 2010). Shorter (longer) whiskers will tend to respond more strongly to components of vortices and wakes that contain higher (lower) frequency stimuli. At the same time, undulations along the whisker length will tend to

reduce vortex-induced vibrations of the whisker, thereby improving tracking (Ginter et al., 2012; Hanke et al., 2010).

The mechanical response of a seal whisker will also depend on how it is oriented on the animal's face. Three parameters are particularly important: the orientation of the whisker's diameter major axis (its "diameter orientation"); the orientation of the whisker's intrinsic curvature (its "curvature orientation," quantified here as ζ_w), and its horizontal emergence angle (θ_w). Vibrations will be larger when the wide, rather than thin, diameter of the whisker faces into the flow (Murphy et al., 2013). Flow stimuli will encounter a gradient of whisker twist angles (ζ_w) across the array, potentially helping the animal extract vortex features and flow direction. Changing whisker curvature orientation will change the magnitude of bending and vibration (Yu et al., 2016b) as well as vibration frequency (Murphy et al., 2013). For a seal swimming forwards, changes in θ_w change the angle of attack of the whisker, effectively changing the area projected into the flow, and thus how the whisker vibrates. Intriguingly, for the seal -- but not for the rat -- the two angles θ_w and ζ_w are strongly correlated (Figs. 6CI). By varying these two angles virtually in lock step across the array, the seal vibrissal system may ensure that these two different sources of vibration variability are always related in the same way.

Finally, the mechanics of wake-following behavior will depend strongly on the seal's active tracking motions, which will change based on the structure of the external wakes the seal senses. In other words, wake-following is a closed-loop sensorimotor behavior in which both sensory and motor structures have co-evolved based on the requirement to sense the features of wakes most salient to efficient predation.

4.9. The increasing importance of whole-body biomechanical models

The fields of neuroscience and bioinspired robotics increasingly recognize the importance of quantifying, simulating, and modeling natural behavior using whole-body biomechanical models (Bolaños et al., 2021; Zweifel et al., 2021). The arrangement of an animal's sensors and muscles determine the neural signals that the animal will obtain. To understand neural control of sensory acquisition behaviors it is particularly important to study closed-loop behaviors within natural environments, an approach increasingly possible in simulation, provided accurate 3D models exist. We anticipate that the present work will be useful for developing underwater seal-like robots for wake detection and tracking, and for studying the biomechanics and neurobiology of these behaviors. For example, the model of the seal array developed here has already been used in fluid mechanics simulations (Liu, 2022) to explore how the pattern of signals received by the whiskers reflects flow structure.

ACKNOWLEDGMENTS

We thank Dr. Christine Scholtyßeck for help handling the seals. E. Claire Mosier, an undergraduate student in Northwestern's Biomedical Engineering department, helped us take some of the data in Rostock. We are grateful to RAPIDFORM™ for providing a temporary stand-alone license to acquire and analyze the scans when we briefly lost access to the internet at a critical point in the work. We thank Yifu Luo for remaking several of the figures. Portions of this work have been published in two Ph.D. dissertations: Graff, MM (2016) *Mechanisms of Whisker Based Flow Sensing*, Ph.D. Thesis, Northwestern University. ProQuest/UMI, 130 pages (Publication No. 10160640). Belli, HM (2017) *Sensing with Whiskers: From Geometry and Mechanics to the Statistics of the Array*, Ph.D. Thesis, Northwestern University, ProQuest/UMI, 253 pages (Publication No. 10681095).

COMPETING INTERESTS

No competing interests declared.

FUNDING

This multi-year research project was sequentially supported by National Science Foundation awards IOS-0846088, CRCNS-IIS-1208118, BCS-1734981 and National Institutes of Health R01-NS116277 to MJZH; by a grant from the VolkswagenStiftung to GD; and by a grant from the German Research Foundation (SPP1207) to GD (DE 538/9-2) and W. Hanke (HA 4411/8-1). H.M.B. was supported in part by an NIH Ruth L. Kirschstein National Research Service Award (F31-NS-090872-01A1) and by an NIH TL1 Clinical and Translational Post-Doctoral Fellowship (TL1TR001447). C.S.B. was supported in part by NSF IGERT: Integrative Research in Motor Control and Movement (DGE-0903637) and by the NIH(T32HD-057845).Open Access funding provided by Northwestern University. Deposited in PMC for immediate release.

References

Ahl, A. S. (1986). The role of vibrissae in behavior - a status review. *Veterinary Research Communications* **10**, 245-268.

Belli, H. M., Bresee, C. S., Graff, M. M. and Hartmann, M. J. Z. (2018). Quantifying the three-dimensional facial morphology of the laboratory rat with a focus on the vibrissae. *Plos One* **13**, 31.

Bolaños, L. A., Xiao, D., Ford, N. L., LeDue, J. M., Gupta, P. K., Doebeli, C., Hu, H., Rhodin, H. and Murphy, T. H. (2021). A three-dimensional virtual mouse generates synthetic training data for behavioral analysis. *Nat Methods* **18**, 378-381.

Bookstein, F. L. (2018). A Course in Morphometrics for Biologists Cambridge University Press.

Boubenec, Y., Shulz, D. E. and Debrégeas, G. (2012). Whisker encoding of mechanical events during active tactile exploration. *Frontiers in Behavioral Neuroscience* **6**.

Brecht, M., Preilowski, B. and Merzenich, M. M. (1997). Functional architecture of the mystacial vibrissae. *Behavioural Brain Research* **84**, 81-97.

Bresee, C. S., Belli, H. M., Luo, Y. and Hartmann, M. J. Z. (2023). Comparative morphology of the whiskers and faces of mice (*Mus musculus*) and rats (*Rattus norvegicus*). *Journal of Experimental Biology* **226**.

Burns, J. (2009). Harbor Seal and Spotted Seal: *Phoca vitulina* and *P. largha*. In *Encyclopedia of Marine Mammals (Second Edition)*, eds. W. F. Perrin B. Würsig and J. G. M. Thewissen), pp. 533-542.

Carvell, G. E. and Simons, D. J. (1990). Biometric Analyses of Vibrissal Tactile Discrimination in the Rat. *Journal of Neuroscience* **10**, 2638-2648.

Carvell, G. E., Simons, D. J., Lichtenstein, S. H. and Bryant, P. (1991). Electromyographic Activity of Mystacial Pad Musculature During Whisking Behavior in the Rat. *Somatosensory and Motor Research* **8**, 159-164.

Danforth, C. H. (1925). Hair in its relation to questions of homology and phylogeny. *American Journal of Anatomy* **36**, 47-68.

Dehnhardt, G. and Kaminski, A. (1995). Sensitivity of the Mystacial Vibrissae of Harbor Seals (Phoca-Vitulina) for Size Differences of Actively Touched Objects. *Journal of Experimental Biology* **198**, 2317-2323.

Dehnhardt, G., Mauck, B. and Bleckmann, H. (1998). Seal whiskers detect water movements. *Nature* **394**, 235-236.

Dehnhardt, G., Mauck, B., Hanke, W. and Bleckmann, H. (2001). Hydrodynamic trail-following in harbor seals (Phoca vitulina). *Science* **293**, 102-104.

Dörfl, J. (1982). The musculature of the mystacial vibrissae of the white mouse. *J Anat* **135**, 147-54.

Ginter, C. C., DeWitt, T. J., Fish, F. E. and Marshall, C. D. (2012). Fused Traditional and Geometric Morphometrics Demonstrate Pinniped Whisker Diversity. *PLoS One* **7**.

Ginter, C. C., Fish, F. E. and Marshall, C. D. (2010). Morphological analysis of the bumpy profile of phocid vibrissae. *Marine Mammal Science* **26**, 733-743.

Grant, R., Wieskotten, S., Wengst, N., Prescott, T. and Dehnhardt, G. (2013a). Vibrissal touch sensing in the harbor seal (Phoca vitulina): how do seals judge size? *Journal of Comparative Physiology a-Neuroethology Sensory Neural and Behavioral Physiology* **199**, 521-533.

Grant, R. A., Haidarliu, S., Kennerley, N. J. and Prescott, T. J. (2013b). The evolution of active vibrissal sensing in mammals: evidence from vibrissal musculature and function in the marsupial opossum Monodelphis domestica. *Journal of Experimental Biology* **216**, 3483-3494.

Haidarliu, S., Kleinfeld, D., Deschenes, M. and Ahissar, E. (2015). The Musculature That Drives Active Touch by Vibrissae and Nose in Mice. *Anatomical Record-Advances in Integrative Anatomy and Evolutionary Biology* **298**, 1347-1358.

Haidarliu, S., Simony, E., Golomb, D. and Ahissar, E. (2010). Muscle Architecture in the Mystacial Pad of the Rat. *Anatomical Record-Advances in Integrative Anatomy and Evolutionary Biology* **293**, 1192-1206.

Hanke, W., Witte, M., Miersch, L., Brede, M., Oeffner, J., Michael, M., Hanke, F., Leder, A. and Dehnhardt, G. (2010). Harbor seal vibrissa morphology suppresses vortex-induced vibrations. *Journal of Experimental Biology* **213**, 2665-2672.

Hans, H., Miao, J. M., Triantafyllou, M., Weymouth, G. and Ieee. (2013). Whisker-like Geometries And Their Force Reduction Properties. In *MTS/IEEE OCEANS Conference*. Bergen, NORWAY.

Hartmann, M. J., Johnson, N. J., Towal, R. B. and Assad, C. (2003). Mechanical characteristics of rat vibrissae: Resonant frequencies and damping in isolated whiskers and in the awake behaving animal. *Journal of Neuroscience* **23**, 6510-6519.

Hires, S. A., Schuyler, A., Sy, J., Huang, V., Wyche, I., Wang, X. and Golomb, D. (2016). Beyond cones: an improved model of whisker bending based on measured mechanics and tapering. *Journal of Neurophysiology* **116**, 812-824.

Hirons, A. C., Schell, D. M. and St Aubin, D. J. (2001). Growth rates of vibrissae of harbor seals (*Phoca vitulina*) and Steller sea lions (*Eumetopias jubatus*). *Canadian Journal of Zoology-Revue Canadienne De Zoologie* **79**, 1053-1061.

Hyvarinen, H. (1989). Diving in Darkness: Whiskers as Sense-Organs of the Ringed Seal (Phoca hispida saimensis). *Journal of Zoology* **218**, 663-678.

Knutsen, P. M., Biess, A. and Ahissar, E. (2008). Vibrissal kinematics in 3D: Tight coupling of azimuth, elevation, and torsion across different whisking modes. *Neuron* **59**, 35-42.

Kruger, Y., Hanke, W., Miersch, L. and Dehnhardt, G. (2018). Detection and direction discrimination of single vortex rings by harbour seals (*Phoca vitulina*). *Journal of Experimental Biology* **221**, 12.

Liu G, J. W., Zheng X, and Xue Q. (2022). Flow-signal correlation in seal whisker array sensing. *Bioinspiration & Biomimetics* **17**.

Luo, Y. and Hartmann, M. J. Z. (2023). On the intrinsic curvature of animal whiskers. *PLoS One* **18**, e0269210.

Meredith, R. W., Janecka, J. E., Gatesy, J., Ryder, O. A., Fisher, C. A., Teeling, E. C., Goodbla, A., Eizirik, E., Simão, T. L. L., Stadler, T. et al. (2011). Impacts of the Cretaceous Terrestrial Revolution and KPg Extinction on Mammal Diversification. *Science* **334**, 521-524.

Miersch, L., Hanke, W., Wieskotten, S., Hanke, F. D., Oeffner, J., Leder, A., Brede, M., Witte, M. and Dehnhardt, G. (2011). Flow sensing by pinniped whiskers. *Philosophical Transactions of the Royal Society B-Biological Sciences* **366**, 3077-3084.

Muchlinski, M. N. (2006). The anatomy of the infraorbital foramen: Implications for interpreting the ecology of extinct and extant primates. *American Journal of Primatology* **68**, 114-115.

Muchlinski, M. N. (2010a). A comparative analysis of vibrissa count and infraorbital foramen area in primates and other mammals. *Journal of Human Evolution* **58**, 447-473.

Muchlinski, M. N. (2010b). Ecological Correlates of Infraorbital Foramen Area in Primates. *American Journal of Physical Anthropology* **141**, 131-141.

Muchlinski, M. N., Durham, E. L., Smith, T. D. and Burrows, A. M. (2013). Comparative histomorphology of intrinsic vibrissa musculature among primates: implications for the evolution of sensory ecology and "face touch". *American Journal of Physical Anthropology* **150**, 301-312.

Muchlinski, M. N., Wible, J. R., Corfe, I., Sullivan, M. and Grant, R. A. (2020). Good Vibrations: The Evolution of Whisking in Small Mammals. *Anatomical Record-Advances in Integrative Anatomy and Evolutionary Biology* **303**, 89-99.

Mugnaini, M., Mehrotra, D., Davoine, F., Sharma, V., Mendes, A. R., Gerhardt, B., Concha-Miranda, M., Brecht, M. and Clemens, A. M. (2023). Supra-orbital whiskers act as wind-sensing antennae in rats. *PLoS Biol* **21**, e3002168.

Murphy, C. T., Eberhardt, W. C., Calhoun, B. H., Mann, K. A. and Mann, D. A. (2013). Effect of Angle on Flow-Induced Vibrations of Pinniped Vibrissae. *PLoS One* **8**.

Neimark, M. A., Andermann, M. L., Hopfield, J. J. and Moore, C. I. (2003). Vibrissa resonance as a transduction mechanism for tactile encoding. *Journal of Neuroscience* **23**, 6499-6509.

O'Leary, M. A., Bloch, J. I., Flynn, J. J., Gaudin, T. J., Giallombardo, A., Giannini, N. P., Goldberg, S. L., Kraatz, B. P., Luo, Z. X., Meng, J. et al. (2013). The placental mammal ancestor and the post-K-Pg radiation of placentals. *Science* **339**, 662-7.

Petersen, R. S., Rodriguez, A. C., Evans, M. H., Campagner, D. and Loft, M. S. E. (2021). A system for tracking whisker kinematics and whisker shape in three dimensions (vol 16, e1007402, 2020). *PLoS Computational Biology* **17**.

Pocock, R. I. (1914). On the facial vibrissae of mammalia. *Proceedings of the Zoological Society of London* 889-912.

Quist, B. W. and Hartmann, M. J. Z. (2012). Mechanical signals at the base of a rat vibrissa: the effect of intrinsic vibrissa curvature and implications for tactile exploration. *Journal of Neurophysiology* **107**, 2298-2312.

Ritt, J. T., Andermann, M. L. and Moore, C. I. (2008). Embodied information processing: Vibrissa mechanics and texture features shape micromotions in actively sensing rats. *Neuron* **57**, 599-613.

Rowe, T. B., Macrini, T. E. and Luo, Z.-X. (2011). Fossil Evidence on Origin of the Mammalian Brain. *Science* **332**, 955-957.

Schulte-Pelkum, N., Wieskotten, S., Hanke, W., Dehnhardt, G. and Mauck, B. (2007). Tracking of biogenic hydrodynamic trails in harbour seals (Phoca vitulina). *Journal of Experimental Biology* **210**, 781-787.

Shui, W., Profico, A. and O'Higgins, P. (2023). A Comparison of Semilandmarking Approaches in the Analysis of Size and Shape. *Animals* **13**, 1179.

Summarell, C. C. G., Ingole, S., Fish, F. E. and Marshall, C. D. (2015). Comparative Analysis of the Flexural Stiffness of Pinniped Vibrissae. *Plos One* **10**.

Towal, R. B., Quist, B. W., Gopal, V., Solomon, J. H. and Hartmann, M. J. Z. (2011). The Morphology of the Rat Vibrissal Array: A Model for Quantifying Spatiotemporal Patterns of Whisker-Object Contact. *Plos Computational Biology* **7**.

Welker, W. (1964). Analysis of Sniffing of the Albino Rat. *Behaviour* **22**, 223 – 244.

Wieskotten, S., Dehnhardt, G., Mauck, B., Miersch, L. and Hanke, W. (2010). Hydrodynamic determination of the moving direction of an artificial fin by a harbour seal (Phoca vitulina). *Journal of Experimental Biology* **213**, 2194-2200.

Wieskotten, S., Mauck, B., Miersch, L., Dehnhardt, G. and Hanke, W. (2011). Hydrodynamic discrimination of wakes caused by objects of different size or shape in a harbour seal (Phoca vitulina). *Journal of Experimental Biology* **214**, 1922-1930.

Williams, C. and Kramer, E. (2010). The Advantages of a Tapered Whisker. *PLoS ONE* **5**, e8806.

Woolsey, T., Welker, C. and Schwartz, R. (1975). Comparative anatomical studies of the Sml face cortex with special reference to the occurrence of "barrels" in layer IV. *Journal of Comparative Neurology* **164**, 79-94.

Yu, Y., Graff, M. and Hartmann, M. J. Z. (2016b). Mechanical responses of rat vibrissae to airflow. *Journal of Experimental Biology* **219**, 937-948.

Yu, Y. S. W., Graff, M. M., Bresee, C. S., Man, Y. B. and Hartmann, M. J. Z. (2016). Whiskers aid anemotaxis in rats. *Science Advances* **2**, e1600716.

Zweifel, N. O., Bush, N. E., Abraham, I., Murphey, T. D. and Hartmann, M. J. Z. (2021). A dynamical model for generating synthetic data to active tactile behavior in the rat. *Proceedings of the National Academy of Sciences of the United States of America* **118**, 10.